UNIVERSITÀ DEGLI STUDI DI PADOVA

Dipartimento di Fisica e Astronomia "Galileo Galilei"

Master Degree in Astrophysics and Cosmology

Final Dissertation

Internal kinematics of stellar populations in Terzan 5

Thesis supervisor

Prof. Antonino P. Milone

Thesis co-supervisor

Dr. Alessandra Mastrobuono-Battisti

Candidate

Mariasole Maglione

Academic Year 2021/2022

Abstract

Globular clusters are stellar systems populated by up to millions of old stars very tightly gravitationally bound. This gives them their spherical shapes and relatively high stellar densities toward their centers. They are among the oldest objects of the Universe for which we can derive reliable age determinations, old enough to witness the entire history of the Milky Way galaxy. Their absolute ages provide lower limits to the age of the Galactic bulge and the Universe.
Two are the most interesting clusters in the bulge of the Galaxy: Omega Centauri and Terzan 5. The former was studied in many different ways, while Terzan 5 was not, even if previous works suggest that it could be the surviving remnant of one of the primordial building blocks that are thought to merge and form galaxy bulges.
The aim of this project is to study the nearby star cluster Terzan 5 to shed light on a number of phenomena that occurred in the early Universe, like the origin of the Galaxy and the contribution of globular clusters to the cosmic reionization. Specifically, I investigated the internal kinematics of multiple stellar populations in Terzan 5 by combining the observed stellar velocities and N-body simulations. I first exploited the computer program KS2 developed at the Space Telescope Science Institute to derive high-precision photometry and proper motions from archive Hubble Space Telescope multi-epoch images of Terzan 5. This provided me a photometric and an astrometric catalogue which were then used to construct the best Color Magnitude Diagram (CMD) of Terzan 5 so far, corrected for Differential Reddening, and the relative Proper Motions (PMs) of the cluster. The results were used to separate the two populations in Terzan 5, one metal poorer and older and the other metal richer and younger, to constrain rotation and construct velocity dispersion distributions of the distinct populations, together with the calculation of the anisotropy parameter. I then run N-body simulations to reproduce the observed results and infer the kinematic properties of multiple stellar populations in Terzan 5. Results can be useful to put some constraints to the formation mechanisms that are responsible for the formation of globular clusters in the bulge and their role in the assembly of the Galaxy.

Contents

Chapter 1

Introduction

In this first Chapter, I describe the modern view of globular clusters, which are now considered very old and complex stellar systems composed of multiple stellar populations. In Section 1.1 I illustrate the main evidence for MPs, together with some theoretical scenarios that could explain their formation in GCs. Section 1.2 shows the main features and previous results of the Terzan 5 GC and its MPs. Section 1.3 highlights the proposed discriminating scenarios about the formation and evolution of Terzan 5 and its possible role in the assembly of the Galaxy. Finally, section 1.4 summarizes the outline and the aim of the thesis.

1.1 Multipopulations in globular clusters

Globular Clusters (GCs) are among the oldest surviving stellar systems in the Galaxy, and as such, they are considered tracers of the early formation history of the Milky Way (MW). The bulge population of GCs is particularly interesting, as it includes systems with a wide range of properties, with a few cases hosting stellar populations with a range of ages and metallicities.
Until a few years ago, GCs were considered the best approximations of Simple Stellar Populations (SSPs), composed of coeval stars with the same chemical composition (e.g. Renzini & Buzzoni 1986). Indeed, their Color Magnitude Diagrams (CMDs), including those obtained from high-precision Hubble Space Telescope (HST) photometry, were similar to isochrones.
The modern view of a GC is, however, much more complex than the one depicted by this kind of CMD: it is now widely accepted that nearly all GCs are composed of Multiple Populations (MPs), discrete groups of stars with different light-element (C, N, O, Al, Mg) and helium contents. MPs correspond to distinct sequences in CMDs that can be followed continuously at all evolutionary stages. One of the crucial factors that led to the discovery of MPs is the availability of improved techniques for reducing HST photometric data based on the effective point-spread function (ePSF; Section 2.3) introduced by Jay Anderson and collaborators (Anderson and King, 2000). The ePSF allowed to achieve accuracy in measuring positions and magnitudes of stars

that were never reached before, thus making it possible to identify and characterize MPs in a large sample of GCs. Another fundamental ingredient to achieve this result was the introduction of new color combinations sensitive to chemical differences among stars. In the respective CMDs, multiple sequences are clearly recognizable. All the photometric diagrams retrieved so far demonstrate that nearly all GCs host a first population (1G) composed of stars with the same content of light elements as halo field stars at similar metallicity, and one or more second population (2G) of stars enhanced in He, nitrogen (N) and sodium (Na), and depleted in carbon (C) and oxygen (O) (e.g. Milone et al., 2013). 1G stars, in particular, reflect the chemical composition of the pristine material from which GCs formed providing the unique opportunity to study the chemistry of primordial clouds where stars formed at high redshift.
While most GCs are considered monometallic (Type I), variations in heavy elements are observed in some of them (Type II, which are 15-20% of the total number of GCs). These include Terzan 5, which is the subject of this thesis.

1.2 The globular cluster Terzan 5

Terzan 5 is a massive GC in the Galactic bulge. It is located in a region heavily obscured by clouds: due to an extreme variation of reddening along the field of view, it is challenging to disentangle all the different evolutionary sequences of the cluster CMD. It was one of six globulars discovered by the French astronomer Agop Terzan in 1968, then cataloged by the Two-Micron Sky Survey as IRC–20385. It is situated in the Sagittarius constellation in the direction of the Milky Way's center. Terzan 5 follows a pretty unknown orbit around the center of the Galaxy (Baumgardt et al. 2021) and is currently moving towards the Sun with a speed of around 90 km/s.
The absolute magnitude of Terzan 5 is at least $M_V = -7.5$ mag (Ferraro et al. 2009). Its bolometric luminosity is about 800 thousand times that of the Sun, while its mass is $9.35 \pm 0.69 \times 10^5 M_\odot$ (Baumgardt et al. 2021). The small core of Terzan 5, about 0.5 pc in size (Baumgardt et al. 2021), has one of the highest star densities in the galaxy. Its volume mass density exceeds $10^6 M_\odot$ pc^3 (Baumgardt et al. 2021). The cluster also has one of the highest metallicities among the Milky Way's GCs, almost solar: $[Fe/H]$=-0.21 (Ferraro et al. 2009).
This work assumes a projected half-light radius of 0.72 arcmins and a core radius of 0.16 arcmins, as indicated by the 2010 version of the Harris (1996) catalog. More recent results are provided by the Baumgardt et al. (2021) online database: core radius using the Spitzer (1987) definition: 0.51 arcmin; projected half-light radius: 1.86 pc; half-mass radius: 3.77 pc; tidal radius according to eq.8 of Webb et al. (2013): 48.83 pc. Finally, Terzan 5 has a parallax of 0.145 mas (Baumgardt et al. 2021).

1.2.1 Terzan 5 observations

The NASA/ESA Hubble Space Telescope images of Terzan 5 show the cluster in wonderful detail, but it is the chaotic motions of its stars that make it

particularly interesting to astronomers. Terzan 5 has an exceptionally dense core. As a result, it is thought to have one of the highest stellar collision rates for a GC. Many stars are pushed so close together that they form tight binary systems. Images of Terzan 5 were taken with the Wide Field Channel of Hubble's Advanced Camera for Surveys.

1.2.2 Previous studies and hypothesis

The precise evolutionary history of Terzan 5 remains elusive. The SSPs content of the bulge is complex, as it hosts populations from different Galactic components and with distinct chemo-dynamical properties. The situation is exacerbated by difficult observational access due to crowding and severe extinction.
Photometric and spectroscopic studies by Ferraro et al. 2009 and Origlia et al. 2011, 2013 identified the presence of a multi-peak metallicity distribution in Terzan 5. More recently, Ferraro et al. 2016 used HST-based proper motions revealing the existence of two stellar populations widely separated in age. Ferraro et al. 2016 suggest that the mass of Terzan 5 progenitor could have been as high as 10^8 - 10^9 $M_\odot$. Schiavon et al. 2017 showed that the MP phenomenon, characterized by the presence of light element abundance anti-correlations, is present in Terzan 5, indicating that some of its populations have a chemistry similar to that of standard GCs.
Another intriguing property of Terzan 5 concerns the abundance patterns of its members. Ferraro et al. 2016 obtained that the distribution of Terzan 5 stars in the α-Fe plane tracks relatively closely that of the bulge field. Ferraro et al. 2016 showed that the change in the slope (the "knee") of the [α/Fe] vs. [Fe/H] relation occurs at a similar metallicity in the two populations. Such a correlation indicates a similarity in the chemical evolution of the systems, where a decline in the [α/Fe] abundance ratio from the α-enhanced, SN II-enriched, the plateau has historically been attributed to the onset of Type Ia SNe (see Section 1.3.1).
Taylor et al. 2022 presented the chemical abundance analysis of 33 red giant stars belonging to Terzan 5. They confirmed the discovery of two stellar populations with distinct iron abundances: a relatively metal-poor component with [Fe/H] = -0.25 dex and another component with [Fe/H] = +0.27 dex, exceeding in metallicity any known Galactic GC. The two populations also show different [α/Fe] abundance ratios. The metal-poor component has an average [α/Fe] =+0.34 dex, consistent with the canonical scenario for rapid enrichment by core-collapse SNe. The metal-rich component has [α/Fe] =+0.03 dex, suggesting that the gas from which it formed was polluted by both type II and type Ia SNe on a longer timescale. Neither of the two populations shows evidence of the [Al/Fe] over [O/Fe] anti-correlation that is typically observed in Galactic GCs. Taylor et al. 2022 propose that Terzan 5 is not a true GC, but a stellar system with a much more complex history of star formation and chemical enrichment.
Previously, D'Antona et al. 2010 showed that the observed HB morphology is also consistent with a model in which the bright HB is composed of second-generation stars that are metal enriched and with a helium mass fraction larger

than that of first-generation stars populating the fainter part of the HB. Terzan 5 would therefore be anomalous, compared to most "normal" clusters hosting multiple populations, only because its second generation is strongly contaminated by SNe ejecta. D'Antona et al. 2010 said the iron enrichment of the bright HB can be ascribed either to contamination from Type Ia supernova ejecta of the low-iron, helium-rich ejecta of the massive AGB stars of the cluster or to its mixing with gas, accreting on the cluster from the environment, that has been subject to fast metal enrichment due to its proximity with the galactic bulge. The model proposed by D'Antona et al. 2010 requires only a small age difference of $\sim$100 Myr.

1.3 Discriminating scenarios

1.3.1 Scenario I. Terzan 5 is the fossil remnant of a building block of the MW bulge

Galaxy bulge formation has been suggested to occur through the rapid assembly at early epochs, followed by the evolution of a central disc/bar and its interactions on a longer timescale with substructures formed in situ (e.g. Kormendy and Kennicutt 2004). The similarity between Terzan 5 and the bulge field found by Ferraro et al. 2009 was suggested to be indicative of a high mass for the progenitor of Terzan 5, which would in turn suggest that this system was an important contributor to the stellar mass content of the Galactic bulge. The evidence moreover led to the suggestion that Terzan 5 could be the fossil remnant of a primordial building block of the bulge of the MW. The role of a system such as Terzan 5 in this picture has yet to be determined. In this framework, Terzan 5 should to be a Type II GC.

1.3.2 Scenario II: Terzan 5 is a complex stellar system

In the scenario proposed by D'Antona et al. (2010) the two populations in Terzan 5 would be almost coeval and their red giant progenitors would have only a small mass difference or a difference in helium content and metallicity, and not much difference in age. This suggests Terzan 5 is not a Type II GC but a complex stellar system, in agreement also with Taylor et al. 2022 who stated that the cluster is not compatible with the features of the surrounding bulge, thus not possibly descending from a building block of the MW (scenario I).

1.3.3 Scenario III: Terzan 5 is the result of a merger between two distinct previous objects

In the merging scenario, the younger age of the bright HB implies that this population would be more massive or denser than the faint HB, after being condensed through the central part of the cluster. Maybe a difference in the center of the density of the two stellar populations which underwent the merging event are somehow different.

1.4 Outline of the thesis

The aim of this thesis is to investigate the internal kinematics of multiple stellar populations in Terzan 5 globular cluster by combining the observed stellar velocities and N-body simulations to shed light on some phenomena that occurred in the early universe.

The outline of the thesis is the following:

- **Chapter 1**. It provides a description of the MPs phenomenon, with its observational evidence and constraints. In addition, an overview of the current state of the research about Terzan 5 is provided.
- **Chapter 2**. It shows a description of the instrumentation and tools used and the photometric and astrometric data reduction performed on the cluster Terzan 5.
- **Chapter 3**. It illustrates the data analysis and main results in terms of photometry, astrometry, and kinematics of multiple populations on Terzan 5. It contains a description of the methods used to identify distinct populations.
- **Chapter 4**. It presents N-body models to reproduce the observed results and infer the kinematic properties of multiple stellar populations in Terzan 5. Results provide constraints to the formation mechanisms that are responsible for the formation of Globular Clusters and their role in the assembly of the Galaxy.
- **Chapter 5**. It includes a summary of the results of the thesis and a comparison with the most recent works in literature.

Chapter 2

Data reduction

In this Chapter, I describe the data used in this work and the tools used for data reduction. The Chapter is organized as follows. Section 2.1 describes the instrumentation used to obtain the images that I analyzed in the thesis. The dataset is illustrated in Section 2.2. Section 2.3 describes the procedure to derive high-precision astrometry and photometry for Terzan 5. The illustration of the method to derive an accurate Point Spread Function (PSF) and measure the stars in the HST images is included and explained in detail. Section 2.4 contains the procedure used to build a catalog for each filter and epoch. Finally, Section 2.5 is dedicated to the calibration of the magnitudes.

2.1 Instrumentation

The so far highest-precision photometry needed to detect and properly characterize MPs is provided by the Hubble Space Telescope (HST). HST is a space telescope orbiting around the Earth, so avoiding distortions introduced by the atmosphere and providing images with higher resolution than that of the majority of ground-based telescopes. Such performance is fundamental to measuring accurate positions and magnitudes of stars in the crowded environment of globular clusters. Moreover, HST can detect photons with wavelengths inaccessible to ground-based facilities due to the opacity of the atmosphere, providing information in bands that are fundamental to detecting and characterizing MPs, including those inferred from the UV filters. Finally, HST is characterized by CCDs that are also optimized for sensitivity in the red region of the spectrum. HST has a primary mirror of 2.4 m and covers the range of wavelengths from 100 to ∼1700 nm. In order to detect light in different spectral bands, the telescope has onboard different cameras, each with a certain Field of View (FoV), wavelength range and plate scale (ps), described in Table 2.1.

Table 2.1: Summary of the information about the different cameras installed on the HST.

ACS (Advanced Camera for Surveys)

Channel	FoV [arcsec^2]	λ [nm]	ps [arcsec pixel^{-1}]
HRC (High Resolution Channel)	29.1 × 26.1	200-1050	0.027
SBC (Solar Blind Channel)	34.5 × 30.8	115-180	0.032
WFC (Wide Field Channel)	202 × 202	350-1050	0.05

WFC3 (Wide Field Camera 3)

Channel	FoV [arcsec^2]	λ [nm]	ps [arcsec pixel^{-1}]
UVIS (UV and Visible)	160 × 160	200-1000	0.04
NIR (Near InfraRed)	123 × 137	850-1700	0.13

2.2 Dataset

In this work, I used the images taken with ACS-WFC in two different filters, the yellow-red filter F606W and the near-infrared filter F814W, and in three different epochs: September 2003, August 2013, and August 2015. This is the first time that all these epochs are used at the same time to reproduce Terzan 5 photometry. The total exposure times vary from 340 to 360 s for long exposures. The total covered FoV is 3.1-1.4 arcminutes. The main properties of the images used in this work are summarized in Table 2.2.

2.3 Effective PSF photometry

In a typical HST image of a GC, stars appear as relatively isolated point-like sources (Anderson & King 2000). Three parameters are necessary to describe them:

- the center coordinates x, y;
- the total flux f.

Starting from the image, which is a 2-dimensional pixel array, a crucial target for a high-precision photometry consists in deriving x, y and f.

2.3.1 The instrumental Point Spread Function

Finding out accurate positions requires an accurate Point Spread Function (PSF) model. Inaccuracies can lead to systematic errors in stars position measurements whose consequent bias, called pixel-phase error, depends on the location of the star within the pixel. The same stellar profile can be fitted with different PSF models; without knowing a-priori the stellar position, one cannot identify an accurate PSF. However, since the two-dimensional PSF describes how the light of a point-like source (as a star in a GC) is distributed after being processed by a telescope, then each star image is a replica of the PSF, with certain values of x, y and f. The PSF produced by a telescope at its focal plane is called *intstumental PSF* (iPSF): it is impossible to observe it directly,

Table 2.2: Summary of the information about all the HST images from ACS-WFC used in the photometric data reduction of Terzan 5.

IMAGE	DATE	TIME	RA	DEC	FILTER	EXP TIME
j8qe09syq	17/09/03	06:40:08	17d48m04s8	-24:46:45.0	F814W	10
j8qe09szq	17/09/03	06:43:31	17d48m04s8	-24:46:45.0	F606W	340
j8qe09t1q	17/09/03	06:52:22	17d48m04s8	-24:46:45.0	F814W	340
j8qe09t4q	17/09/03	07:06:09	17d48m04s8	-24:46:45.0	F814W	10
jc3801i8q	18/08/13	11:52:42	17d48m04s8	-24:46:44.5	F606W	50
jc3801i9q	18/08/13	11:55:52	17d48m04s8	-24:46:44.5	F606W	365
jc3801ibq	18/08/13	12:04:35	17d48m04s8	-24:46:44.5	F606W	365
jc3801idq	18/08/13	12:13:18	17d48m04s8	-24:46:44.5	F606W	365
jc3801ifq	18/08/13	12:22:01	17d48m04s8	-24:46:44.5	F606W	365
jc3801ihq	18/08/13	12:30:44	17d48m04s8	-24:46:44.5	F606W	365
jc3801ilq	18/08/13	13:26:51	17d48m04s8	-24:46:44.5	F814W	10
jc3801imq	18/08/13	13:29:21	17d48m04s8	-24:46:44.5	F814W	365
jc3801ioq	18/08/13	13:38:04	17d48m04s8	-24:46:44.5	F814W	365
jc3801iqq	18/08/13	13:46:47	17d48m04s8	-24:46:44.5	F814W	365
jc3801isq	18/08/13	13:55:30	17d48m04s8	-24:46:44.5	F814W	365
jc3801iuq	18/08/13	14:04:13	17d48m04s8	-24:46:44.5	F814W	365
jct201g9q	20/04/15	16:36:06	17d48m04s8	-24:46:44.5	F814W	10
jct201gaq	20/04/15	16:38:40	17d48m04s8	-24:46:44.5	F814W	372
jct201gdq	20/04/15	16:47:29	17d48m04s8	-24:46:44.5	F814W	371
jct201gfq	20/04/15	16:56:18	17d48m04s8	-24:46:44.5	F814W	371
jct201ghq	20/04/15	17:05:07	17d48m04s8	-24:46:44.5	F814W	371
jct201gjq	20/04/15	17:13:57	17d48m04s8	-24:46:44.5	F814W	372
jct201goq	20/04/15	18:06:39	17d48m04s8	-24:46:44.5	F606W	50
jct201gpq	20/04/15	18:09:54	17d48m04s8	-24:46:44.5	F606W	398
jct201gsq	20/04/15	18:19:10	17d48m04s8	-24:46:44.5	F606W	397
jct201guq	20/04/15	18:28:25	17d48m04s8	-24:46:44.5	F606W	397
jct201gwq	20/04/15	18:37:39	17d48m04s8	-24:46:44.5	F606W	397

what can actually be observed is an array of pixels, each one with a value of registered counts.

2.3.2 The effective Point Spread Function

A star image is distributed over several pixels. The value of counts in a pixel centered at some offset $(\Delta x, \Delta y)$ from the center of the iPSF, depends on the results of a convolution between the iPSF and the sensitivity profile of a pixel. The *effective PSF* (ePSF), as defined in Anderson and King (2000), consists in this convolution. It gives the fraction of a star light that should fall in each pixel of a star image, taking account of where the center of that pixel lies with respect to the center of the star. The ePSF is a continuous function and it is smoother than the iPSF. The ePSF has three major advantages with respect to the iPSF:

1. it simplifies the calculations: fitting it to a stellar image does not require an integration, but only to adjust the values of centre coordinates and total flux until the sum of the squares of the residuals is minimized.

2. it is easier to solve. Knowing x, y and f of a certain pixel, one can derive at which offset $(\Delta x, \Delta y)$ a certain pixel has sampled the ePSF. If the 3 parameters are known for a large number of pixels, it is possible to obtain a very large number of estimates of ePSF as a function of $(\Delta x, \Delta y)$.

3. the values of ePSF result from integration over the actual pixel sensitivity profile of the detector. Thus, no assumption about sensitivity variations within a pixel is necessary. It represents whatever results from the combination of the detector and iPSF, without assuming anything about any of them.

2.3.3 ePSF for Terzan 5

The techniques presented in Sections 2.3.1 and 2.3.2 are here applied to derive a PSF model for the stars in each exposure of Terzan 5. To derive an appropriate PSF model we would need stellar position and fluxes, but no positions and fluxes can be measured without a PSF model. To break this degeneracy I adopted an iterative procedure.

First of all, I used a ePSF library suitable for the filter and the camera to estimate first-guess positions and magnitudes. Such raw quantities are used to derive an improved PSF model then used to measure stars in the next iteration. Each iteration consisted in three stages:

1. raw positions and magnitudes of each pixel near a star are converted into an estimate of ePSF in the corresponding point;

2. the measured ePSF is used to better estimate, by least-square fitting, the position and magnitude of each star considered;

3. the values found in the previous stage are transferred to a common reference frame, combining them and analyzing the residuals.

There is still a problem regarding the degeneracy between the model and the center position of a star. The bias introduced by the pixel-phase error can be avoided by considering multiple observations of the same star at different dither positions. Averaging the multiple observations makes it possible to obtain a better ePSF profile. These stages are repeated iteratively, improving the model until it basically does not change anymore between two subsequent iterations.

The first iteration allows the building of a model based on the actual image, using the raw positions and magnitudes obtained from fitting the PSF library. To do so, the most isolated and luminous (but not saturated) stars not contaminated by cosmic rays have been considered. This was done using the two Fortran routines `img2psf` (Anderson & King 2000) on all the exposures taken with ACS-WFC per every single epoch. These routines find all the stars in a certain image that meet some criteria, defined by the following arguments:

- HMIN, the minimum distance in pixels between two sources (used: 13);

- FMIN, the minimum counts value of a source (used: 3000);

- PMAX, the maximum counts value of a source (used: 54900, right below the saturation limit);

- QMAX, the maximum value of the Q parameter, an indicator of the quality of the fit. If it is too high, the source fitted is probably not a star (used: 0.4);

- NSIDES, how many regions the image has to be divided. Using a lot of different regions helps to take into account variations of the PSF across the chip. The value was kept at 1 for all the images analyzed;

- PSFFILE, what initial PSF model is used;

- IMG.fits, the image on which the procedure is performed.

At this point another routine has been exploited: `img2xym` (Anderson & King 2006). It uses the just-derived PSF model to obtain positions and magnitudes of all the sources that satisfy some criteria, defined by the values of HMIN, FMIN and PMAX, in a given image. This time a larger number of stars is considered, imposing HMIN = 3, FMIN = 50 and PMAX = 99999. This procedure has to take into account that, because of position-dependent charge diffusion and optical aberrations, the PSF could change shape by changing its position on the detector. For this reason, the software used do not compute a single PSF, but a grid of 9 $\times$ 10 PSFs. An example is given in Figure 2.1. The PSF model for any point in the detector is then obtained by interpolating the PSF among the four nearest grid points. The procedure is applied for each image in each filter in each single epoch, resulting in separate groups of files containing, among other quantities, positions and instrumental magnitudes, given by $m_{ins} = -2.5 \times log(f)$.

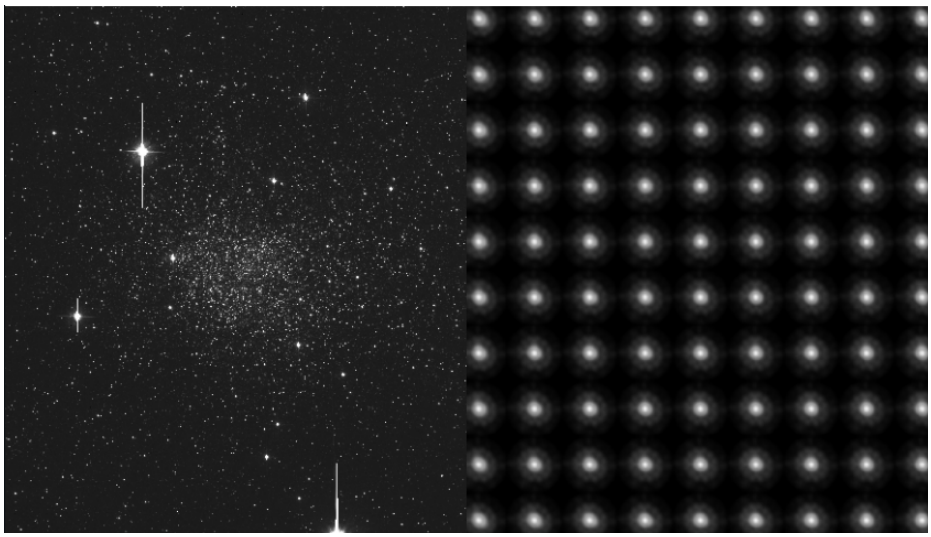

Figure 2.1: In the left panel I represented an exposure of Terzan 5. In the right panel is shown the derived PSF grid.

2.4 Catalogues

Once derived position and magnitude of each star are in all the images, it is possible to build a catalog of stars in Terzan 5. The images can be reduced through two different methods, which use different approaches. In the first one, every image is reduced singularly. Then, for each filter, the information on all the images is put together. In the second one, images in each filter are stacked in a single image. After that, these images are reduced. The first method gives more accurate positions and magnitudes than the second for bright stars, while the second gives more accurate results for faint stars. For this work, I used the first method only. This choice is based on the fact that Terzan 5 stars can be distinguished and characterized mainly in the upper part of the CMD, so the first method gives me the best positions and fluxes with single image analysis (and no signal dilution).

The files obtained in Section 2.3.3 contain sources that fulfilled all the requirements inserted in the routines, but not all are *real* stars. In order to delete from the catalog the unwanted sources, it is important to consider the value of Q. This parameter is a good indicator of the fit quality (telling how much the PSF reproduces a source). The well-reproduced sources are stars. For those ones, Q has a defined dependence from magnitude, being smaller if the source is brighter. Thus, a sort of cleaning process is necessary, as shown in Figure 2.2, keeping only the green stars. During this process, it is important to not clear saturated stars, because they are necessary in the next operations. Therefore, the cleaning is only made for stars with $m > -13.7$ mag.

The next step is to obtain catalogs for the two different filters $F814W$ and $F606W$ per single epoch. To do so I chose an image used as a reference frame, called *master frame*, per each filter and epoch. This is necessary because the different images are not perfectly superimposed. In order to bring each one in the master reference frame, it is used the routine `xym2mat` by Jay Anderson. The aim is to identify the same stars in different images, through two iterations:

1. In the first iteration, the brightest stars of the master frame and in other images (also the saturated ones) are identified. The routine looks for triangles of stars with similar sides ratio between the master and the analyzed image. By finding these triangles, common stars can be identified. Using the coordinates of this group of stars in both the master frame and image reference frame, it calculates by least square fitting the 6 coefficients of the linear transformation that allows changing coordinates:

$$\begin{cases} x_1 = A + Cx_2 + Ey_2 \\ y_1 = B + Dx_2 + Fy_2 \end{cases}$$

   where A, B, C, D, E, F are the coefficients, while (x_1, y_1) and (x_2, y_2) are the coordinates of a star in the two reference frames. Therefore, the positions and magnitudes of each image can be expressed in terms of the master reference frame.

2. Since the saturated stars is not well measured, in building an accurate

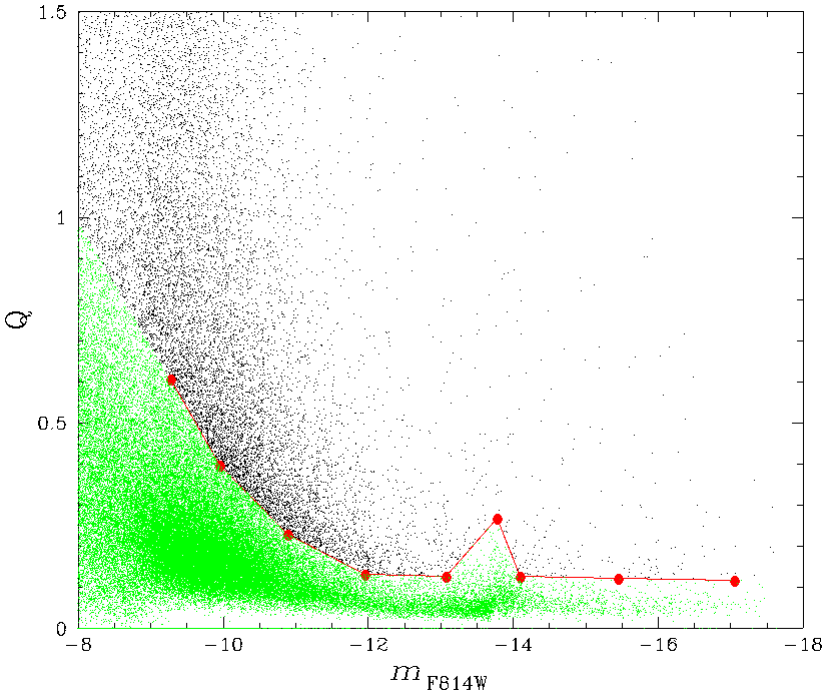

Figure 2.2: Cleaning process for stars in one F814W exposure. The red line, obtained by selecting well-reproduced stars, separates the good stars (in green) and the discarded stars (in black). The magnitude on the x axis is given in the instrumental magnitude units. The bump at -13.8 mag indicates the start of the cleaning process for the second population of stars.

catalog they should not be taken into account. A second iteration is then performed considering only not saturated stars, starting from the transformation derived in the first one. In the procedure, a series of files with the position and magnitude of the common stars and their residuals with respect to the master are obtained. The distribution of the residual of the position is shown in Figure 2.3 as an example. The `xym2mat` routine requires one argument, that is the distance (in pixels) from a star within which the program search for common stars. In the first iteration, the distance is kept quite large, while in the second one is smaller.

After that, it is possible to obtain a catalog for each filter using the routine `xym2bar` developed by Jay Anderson. It calculates the average values of position and magnitude between the common stars. One argument is required: the minimum number or different images in which the same star has to be individuated to be considered. It comes from a compromise between having catalogs with a large number of stars or with a few best-measured stars and depends of course on the number of images available for a given filter. On building these files, all the stars brighter than -6 mag have been considered, avoiding the fainter ones. This is due to the fact that this part of photometric reduction works better for bright stars, while the faints will be analyzed in Section 2.3.2.

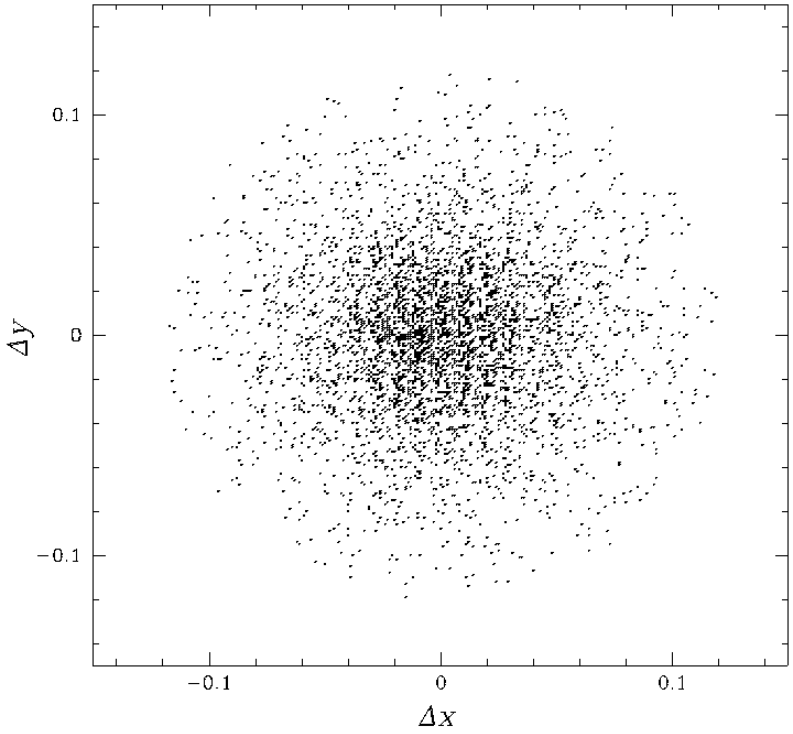

Figure 2.3: Plot of the residuals of the transformation between the master and another image for filter F814W, August 2013. The units are pixels.

The next step is to obtain catalogs with stellar magnitude in different filters. To do so, the routine `xym1mat` by Jay Anderson has been used to link catalogs together. Once chosen a reference catalog (or master frame) is, the software is used to link it with the ones in other filters, finding the corresponding stars (which are not necessarily in the same order in different catalogs). The master here used is the catalog in F814W, epoch August 2013.
The last thing done consisted in expressing the stars' coordinates with respect to an absolute reference frame, the GAIA one. First of all, the catalog of Terzan 5 has been downloaded from the GAIA Data Release 2 (Gaia Collaboration et al. 2018). Since positions from DR2 are expressed in terms of right ascension (RA) and declination (DEC), it has been necessary to transform them into linear coordinates. Then, using again `xym1mat`, the previously obtained catalog in F814W is linked with the GAIA one. A new master frame is now created, with GAIA positions and HST magnitudes. Starting from this one, the `xym2mat` and `xym2bar` procedure is now repeated, obtaining a new F814W catalog. For the F606W filter, which will be linked to the F814W, the obtained catalog and the one in the designed filter have been tied up together using `xym1mat` routine. The master frame in each filter is then given by the GAIA positions and the HST magnitudes. Finally, the `xym2mat` and `xym2bar` procedure is now repeated, obtaining a new catalog for F606W filter. This new catalog has been linked to the F606W one with `xym1mat`. This entire procedure was done per every single epoch: September 2003, August 2013, and April 2015.

2.5 Magnitudes calibration

In order to have a physical meaning, instrumental magnitudes need to be calibrated. The calibrated magnitude is given by the relation:

$$m_{cal} = m_{ins} + \Delta mag + ZP_{filt} + C \tag{2.1}$$

where m_{ins} is the instrumental magnitude, Δmag the difference between the PSF and aperture photometry, ZP_{fit} is the zero-point for a given filter and C is the aperture correction.
In order to find Δmag, the routine `drz_phot_gfortran` has been used. It measures the aperture magnitudes in the images in drz format, which are images of Terzan 5 at an exposure time of 1 s, thus with the values registered in each pixel that are actually the number of counts per unit second. It needs the following arguments: isolation index (HMIN), minimum and maximum flux (respectively FMIN and PMAX), and the image analyzed. The arguments are defined with the aim of considering only bright, isolated, and not saturated stars.
In order to perform the aperture photometry, the aperture radius, inner and outer radius has been defined. They have been chosen to be as large as possible, without including the flux of other nearby sources. The aperture magnitudes are then utilized to estimate Δmag. The procedure is iterative: plotting Δmag vs m_{ins} (obtained from PSF photometry) and considering the brightest and better-measured stars, one can find an average value of Δmag. In the first iteration, an initial by-eye value of Δmag and an interval around it of 4-5 σ (also this one imposed arbitrarily) have been used to select an initial sample of stars. Then, the Δmag median and the σ of the selected stars are calculated. Using these values as the initial ones, the procedure is repeated considering stars within an interval of 2-3 σ, until the result does not change between two subsequent iterations. The final result of these iterations is shown in Figure 2.4.

The values of ZP_{filt} and C can be found from the utility available at

`http://www.stsci.edu/hst/acs/analysis/zeropoints`

for observations in ACS. These values depend on the filter considered, the date of observation and the aperture radius.

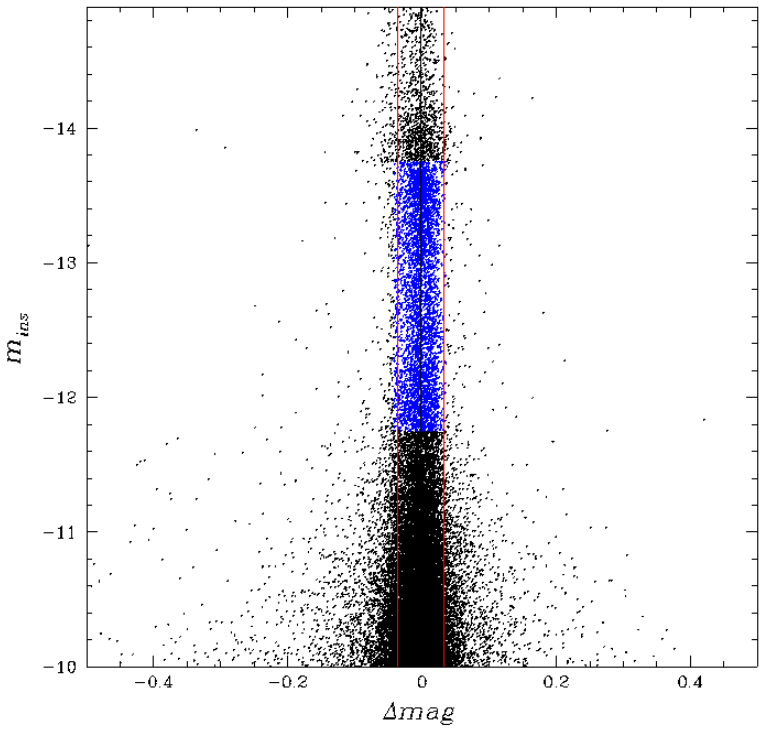

Figure 2.4: Plot of the instrumental magnitude m_{ins} (from PSF photometry) with respect to Δmag, used to find the latter one. The black vertical continuous line in the centre indicates the value of Δmag found from the iterative procedure, while the red lines are located at a distance of $\pm 2\sigma$ from the central one. The blue stars are the ones used to estimate the median. The magnitudes are all given in instrumental magnitude unit.

Chapter 3

Data analysis and main results

In this Chapter, I analyze the photometric and astrometric catalogs derived in the previous Sections to identify and characterize for the first time the MPs in Terzan 5. The Chapter is organized as follows. Section 3.1 shows the CMD for Terzan 5 and describes the procedure adopted to correct the effect of Differential Reddening (DR) on the photometry. A final CMD, with the field removed and corrected for DR, is also given. Section 3.2 presents the relative PMs for Terzan 5 gained through the astrometric catalog derived from HST data. Section 3.3 includes the method used to separate the two populations, one metal richer and younger and the other metal poorer and older (previously identified as two separated populations by Ferraro et al. 2009). It includes a CMD with the populations depicted in different colors. Section 3.4 depicts the density variation from the center of the cluster of the two populations, showing the metal richer is more concentrated. The isodensity diagrams and center of mass calculations are included. Finally, Section 3.5 describes the internal kinematics of multiple populations through velocity dispersions analysis and anisotropy calculations.

3.1 CMDs and DR correction

From the calibrated photometric catalog obtained with the previous steps, I was able to retrieve the CMD for Terzan 5. However, as presented in Figure 3.1, I had to remove the field stars belonging to the Galactic bulge. The selections I did are:

- Stars with good position measurements, where "good" means the square root of the quadratic sum of the uncertainties $\Delta x, \Delta y$ on the measurements should be low: $err = \sqrt{\Delta x^2 + \Delta y^2} < 3$, with 3 chosen by eye after computing the distribution of Δx as a function of Δy;
- Stars with good proper motions, where "good" means the square root of the quadratic sum of the residuals dx, dy on the proper motions should be low: $dr = \sqrt{dx^2 + dy^2} < 0.5$, where 0.5 was chosen by eye after computing the distribution of dx as a function of dy;

- Stars with a magnitude $m_{F814W} < -10$;
- Stars measured by HST at least in two of the three epochs.

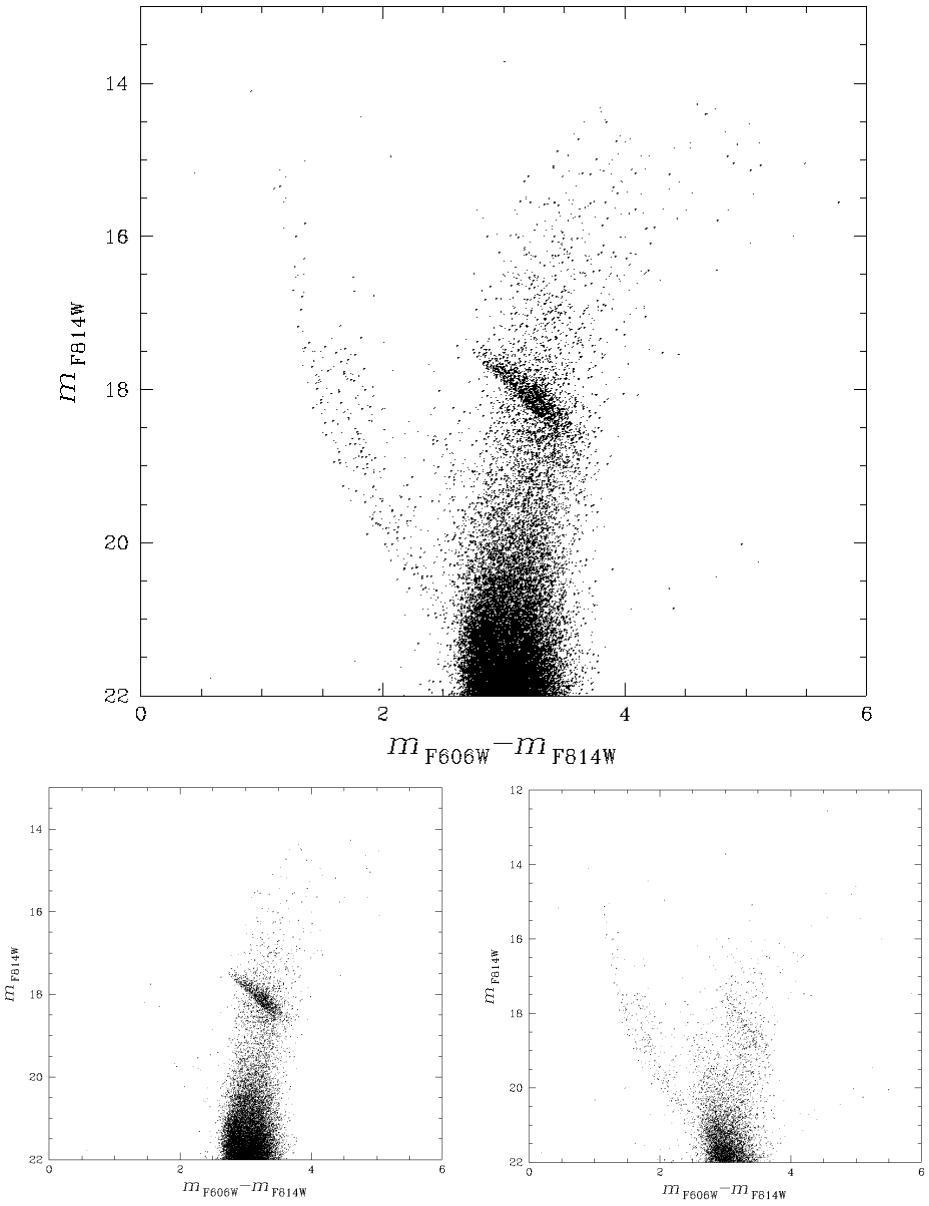

Figure 3.1: Calibrated CMD of the cluster and the field stars from the bulge (upper panel), of the cluster cleaned from the field (lower left panel) and of the bulge stars that have been removed (lower right panel). The magnitudes are given in the instrumental unit.

Actually, the CMD in the central panel of Figure 3.1 is not the final one: it is heavily affected by the reddening. This is due to the position of Terzan 5 in the bulge of the Milky Way, a region highly obscured by clouds and interstellar dust that cause absorption of the light emitted from astronomical objects. This interstellar absorption A_X in a given band X is larger at smaller wavelengths λ, and equal to the difference between the apparent magnitude m_{app} and the original magnitude m_0:

$$A_X = m_{app} - m_0 \tag{3.1}$$

Since the difference between the apparent magnitude of a star in two different bands X_1 and X_2 is expressed by the color excess:

$$E(X_1 - X_2) = A_{X_1} - A_{X_2} \tag{3.2}$$

if $\lambda_{X_1} < \lambda_{X_2}$, then considering observations where $X_1 = B$ and $X_2 = V$ we can call this color excess $E(B-V)$ with the name of reddening. A direct relation between the absorption parameter and the reddening is given by:

$$A = k \times E(B - V) \tag{3.3}$$

with k depending on the filter. For HST data in the filters used for this work: $k_{F814W} = 1.8420$, $k_{F606W} = 2.8782$.

The interstellar reddening is not constant, but changes with the direction of the line of sight. When we observe a GC, small differences of $E(B\text{-}V)$ across the FoV of an observation, referred to as DR, produce an artificial spread in a typical evolutionary sequence of the CMDs. As a consequence, DR can dramatically reduce the amount of information on the properties of stellar populations of a cluster that we can infer photometrically.
In order to minimize the impact of DR on our photometry, we adopted the procedure for DR correction introduced by Milone et al. (2012b). This method is explained in Figure 3.2, using NGC 2298 as a template.

Panel (a) displays the CMD, where cluster stars are plotted as grey points. The red arrow represents the reddening vector and defines a new reference system, where the "abscissa" is parallel to the reddening vector direction and the "ordinate" is perpendicular to it. The two dotted lines define a subsample of cluster stars (black points) used for the computation of the DR. In panel (b) the selected stars are represented in the new reference system. The dashed red line marks the fiducial line of the cluster stars. This fiducial line is obtained by dividing the interesting region of the CMD in small-magnitude bins and interpolating the values of the median of the color and magnitude of stars in each bin. Panel (c) displays the difference between the color of each star and that of the fiducial line, Δ "abscissa". The subsample of stars used is located in a region of the CMD where the angular separation between the evolutionary sequence and the direction of the reddening vector is maximum. In this portion of the CMD, indeed, the impact that the random magnitude errors have on the observed color spread is minimum when compared with the effect of DR. Then, the DR value of each cluster star is estimated as the median value of the Δ "abscissa" scatter of the 30–100 closest spatial neighbor star. This quantity is an estimate of the DR that affects that star. This procedure was applied to Terzan 5. Figure 3.3 shows the bimodal distribution of stars in the Red Clump (RC) and Horizontal Branch (HB) in the direction orthogonal to the reddening vector.

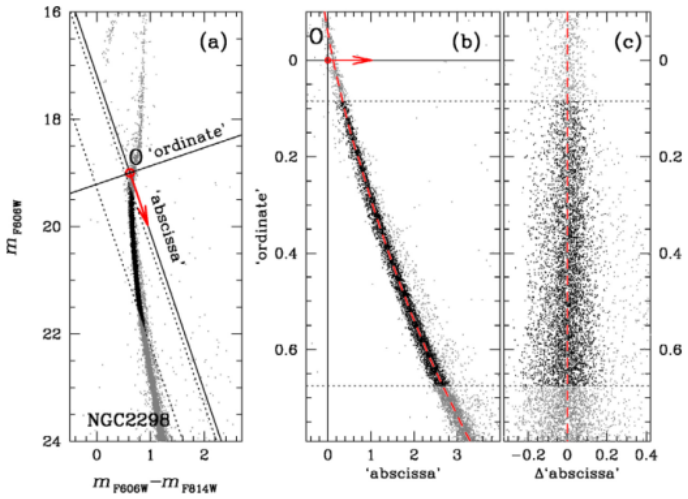

Figure 3.2: Method for the correction of DR in the photometry of NGC2298 (from Milone et al. 2012c). The red arrow in panel (a) indicates the direction of reddening. The continuous black lines are "abscissa" and "ordinate" of the reference frame introduced in the procedure. The dotted lines define an interval within which the subsample of stars is selected. The position of NGC 2298 stars in this reference frame is shown in panel (b) where the fiducial line of the MS is drawn as a dashed red line. Panel (c) shows the "ordinate" vs. Δ "abscissa" diagram.

The final CMD, corrected for DR, as is shown in Figure 3.4, together with the CMD for the field stars which were removed.

Note that the color width of the RGB is significantly reduced in the DR-corrected CMD, as well as the color and magnitude of the cluster HB stars, which appears more defined in the DR-corrected CMD. Moreover, the RC is clearly visible in the DR-corrected CMD as an overdensity of stars at m_{F606W}-m_{F814W} between 3 and ∼3.4 mag and m_{F814W} ∼18 mag.

3.2 Relative proper motions for Terzan 5

From the final astrometric catalog retrieved with the data reduction on HST images, I was able to compute a plot of the Proper Motions (PMs) distribution for the stars in Terzan 5. This is shown in the left panel of Figure 3.5. Then all the saturated sources were excluded, together with imposing a low residual of the PM with the definition given at the beginning of Section 3.1. They are *relative* PMs, because related to the average local cluster motion.
To create these plots, I converted the PMs into units of mas yr^{-1} by multiplying the measured displacements by the pixel scale of the master frame (0".04pixel^{-1}). Since the master frame has been oriented according to the equatorial coordinate system, the PM along x direction corresponds to that projected along the right ascension $R.A$, defined as $\mu_\alpha cos\delta$, while the PM component along the y coordinate corresponds to that projected along the declination DEC defined as μ_δ.

The first clear feature appearing from the plot containing the PMs of the cluster

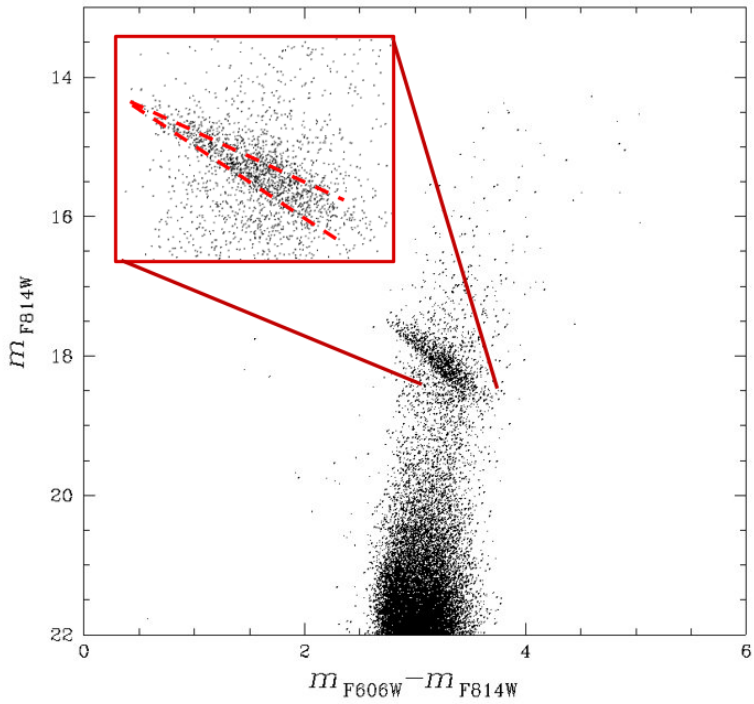

Figure 3.3: Calibrated CMD for Terzan 5 with a highlight of the Horizontal Branch and Red Clump's stars. Here we can recognize the broad color and magnitude distribution of stars in the direction orthogonal to the reddening vector, which let us apply the procedure for DR correction developed by Milone et al. 2012. The magnitudes are given in the instrumental magnitude unit.

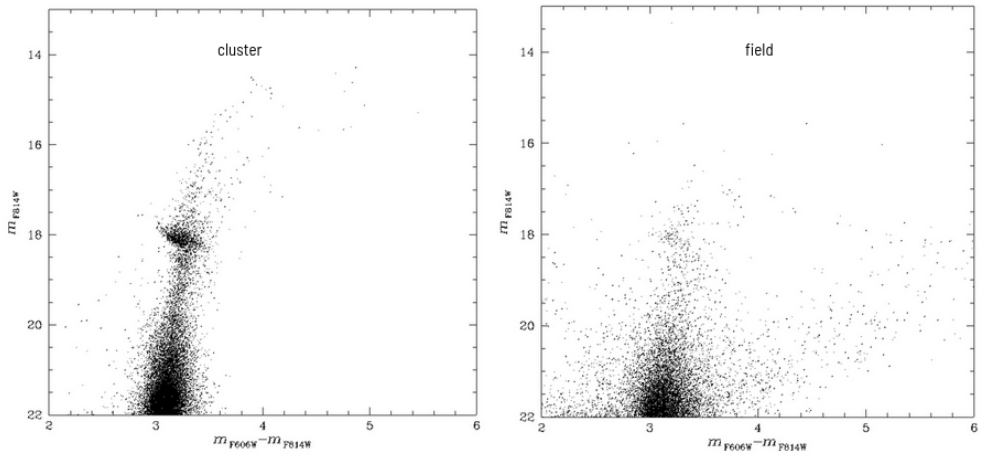

Figure 3.4: Final CMD for Terzan 5 with calibrated magnitudes and corrected for differential reddening (left panel) and CMD of the field stars, removed with the previously listed selections, corrected for DR (right panel). All the magnitudes are given in the instrumental magnitude unit.

(right panel in Figure 3.5) is that more than 70% of the stars are distributed within the innermost 1.5 mas yr^{-1}. The remaining fraction of stars describes a sparser and asymmetric distribution out to about 10 mas yr^{-1}. This is

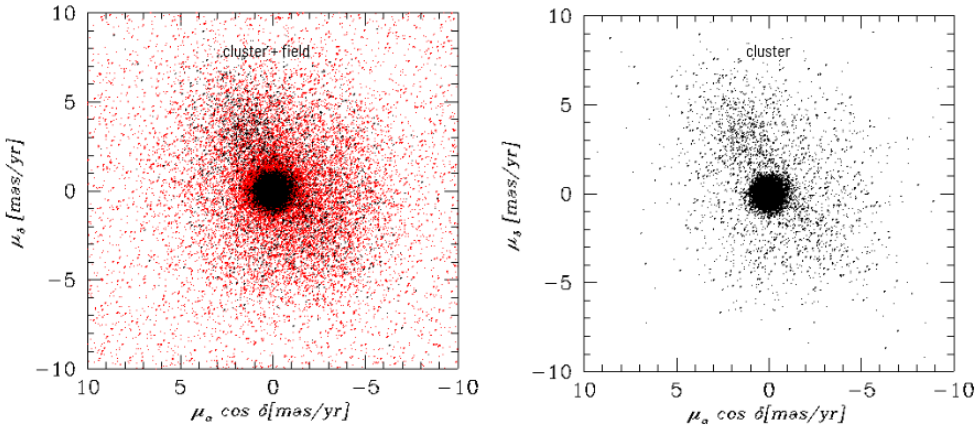

Figure 3.5: PMs projected along the *R.A.* and *DEC* for Terzan 5 (left panel) together with field stars, printed in red, and PMs of the cluster stars only (right panel). These PMs are relative to the local cluster motion.

consistent with the results obtained on the PMs of Terzan 5 by Massari et al. 2015 using the ACS-WFC and WFC3 images of HST from the epochs September 2003 and August 2013, two of the three used in this work.
I did not retrieve the absolute motion of Terzan 5 stars from cross-correlating my PMs catalog with other public catalogs of stellar PMs. Just applying a shift in the PMs plot to re-center the data not with the local cluster motion but with Hubble zero center, I obtained the plot shown in Figure 3.6.

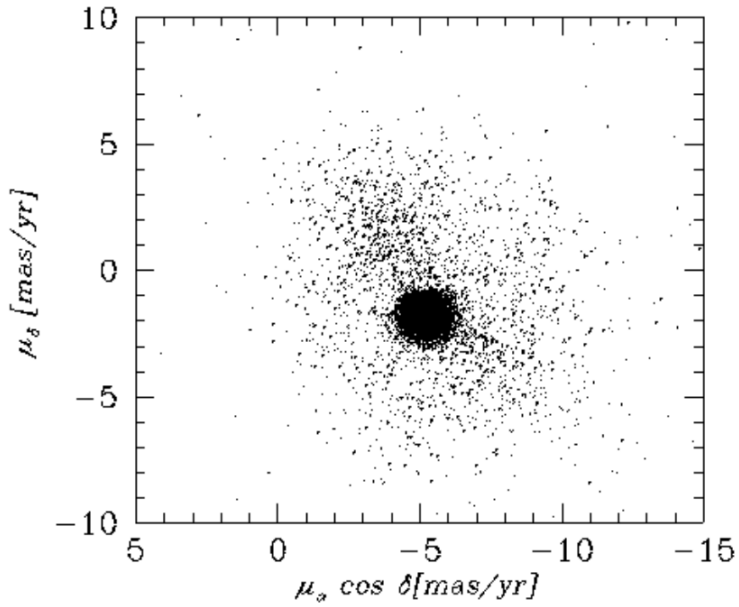

Figure 3.6: Absolute PMs for Terzan 5.

3.3 Selections of the two populations

Terzan 5 is characterized by two separate populations, as described in section 1.2. In order to separate the two populations, I considered the photometric catalog in filters $F814W$ and $F606W$ from ACS-WFC observations retrieved before, and then added the K-band photometry made from ground-based images by using MAD (Multi-Conjugate Adaptive Optics) demonstrator instrument installed at the Very Large Telescope (VLT) of the European Southern Observatory (ESO), by Ferraro et al. 2009. MAD operates at near-infrared wavelengths, thus revealing the only component of stellar radiation that can efficiently cross the thick clouds of dust obscuring the Galactic bulge. It is able to perform exceptionally good and uniform adaptive optics correction over its entire field of view (1'×1'), thus compensating for the degradation effects to the astronomical images induced by the Earth's atmosphere. The set of K-band (2.2μm) images of Terzan 5 is close to the diffraction limit. The sharpness and uniformity of the images yield very high quality photometry, resulting in accurate separation of the two HB red clumps, separated in luminosity: a bright horizontal branch at K = 12.85 and a faint horizontal branch at K = 13.15, the latter having a bluer color.
The selection made on the basis of the K data, the same used by Ferraro et al. 2009 when discovering the two populations, is better than the one made in optical, for the stars observed in the K band. This is simply because the K filter separates the two red clumps better. However, these K-band data present the disadvantage of having a very limited range in terms of distance from the center (corresponding to less than a thousand pixels with respect to HST images). Then as a compromise, to analyze the outermost part, I made similar selections by eye based on the Terzan 5 CMD corrected for DR (in which we have a hint of the two red clumps). At this point, the selections for the stars observed in the K band and the selections for the remaining stars observed with HST in visible/near-infrared bands are put together in order to separate the populations. Precisely, I considered a star metal-rich or metal-poor if it has been selected as such in the K band data (regardless of its classification in optical), and if the star was not observed in K, then I used the classification made in optical. The RCs and RGBs were associated (as shown in Figures 3.7 and 3.8) as follows:

- **Metal Poor** (MP) population: fainter RC, bluer RGB;
- **Metal Rich** (MR) population: brighter RC, redder RGB.

The lower part of the CMD could not be separated.

The final separation of the multipopulations in Terzan 5 is shown in figure 3.9, where the metallicity as retrieved by Ferraro et al. 2009 is also indicated. The left panel shows the stars belonging to the metal richer population colored in red, the right panel the stars belonging to the metal poorer population colored in blue. This kind of separation was never done before for Terzan 5.

At this point, in Figure 3.10 the final CMD for Terzan 5 with the two populations separated in different colors (always, red for MR, blue for MP) is

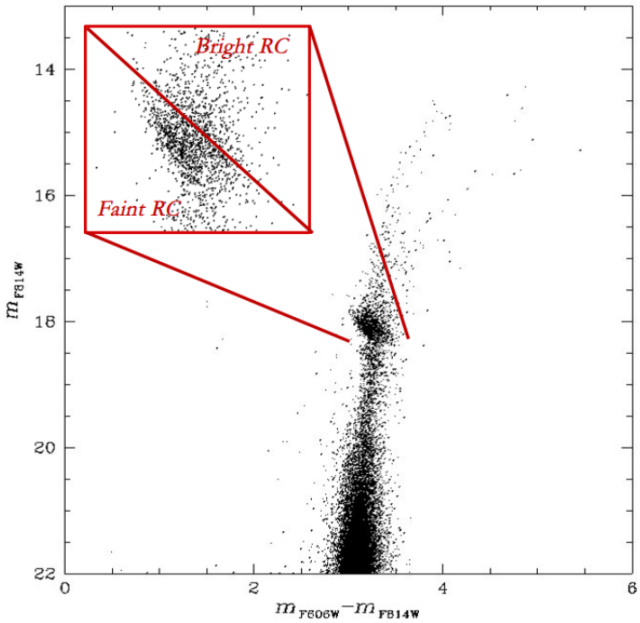

Figure 3.7: Separation of the two red clumps in Terzan 5, one fainter and one brighter. The selections are based on the optical photometric catalog retrieved from ACS-WFC images of HST and on the infrared dataset in the K band retrieved with MAD on the VLT. The magnitudes are given in the instrumental magnitude unit.

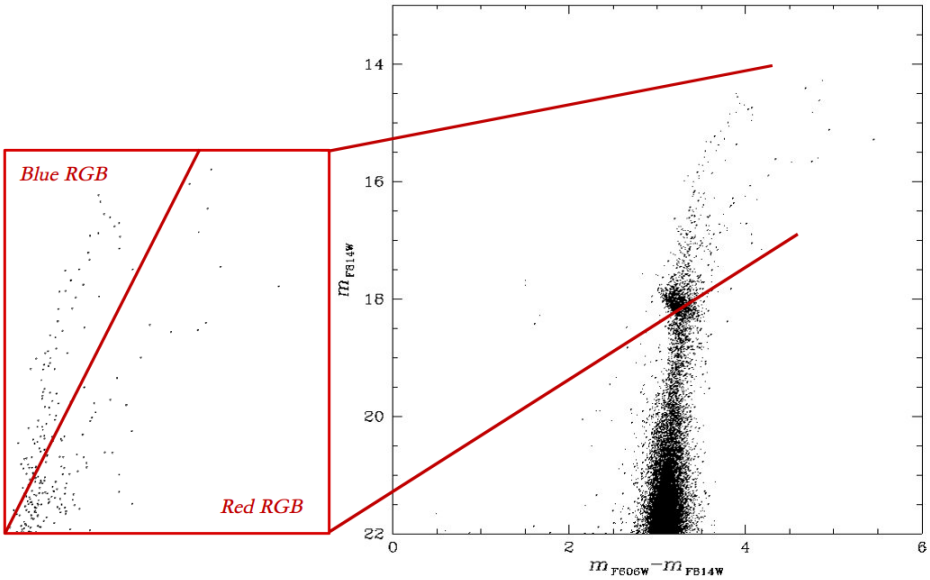

Figure 3.8: Separation of the two red giant branches in Terzan 5, one bluer and one redder. The selections are based on the optical photometric catalog retrieved from ACS-WFC images of HST and on the infrared dataset in the K band retrieved with MAD on the VLT. The magnitudes are given in instrumental magnitude unit.

depicted.

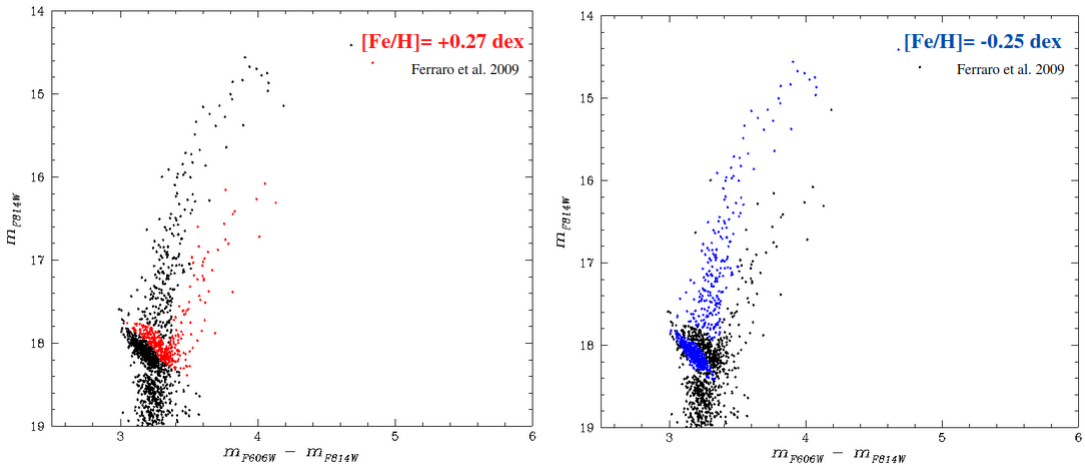

Figure 3.9: Separation of the populations in Terzan 5: one metal richer (left panel) and one metal poorer (right panel). The magnitudes are given in the instrumental magnitude unit.

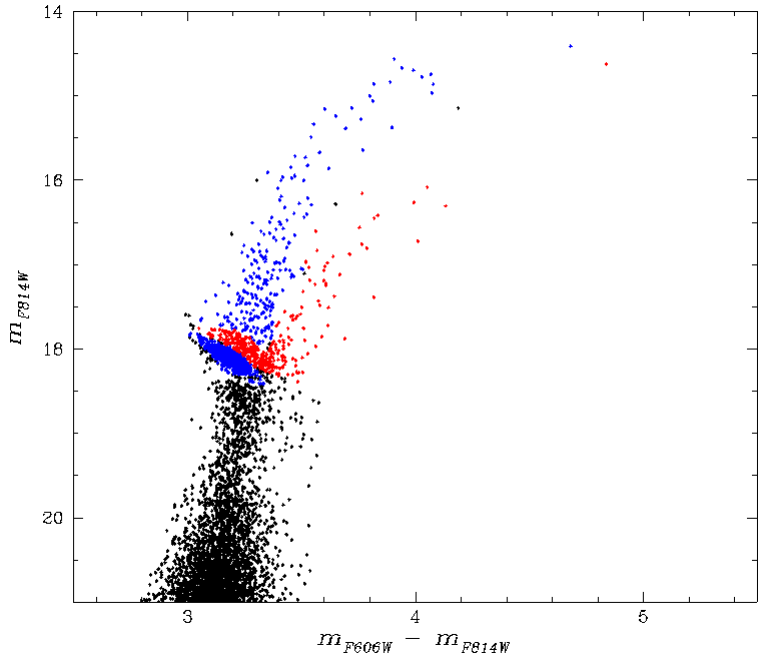

Figure 3.10: CMD for Terzan 5 with the two populations separated. The metal richer is shown in red, and the metal poorer in blue. The magnitudes are given in the instrumental magnitude units.

3.4 Density distribution

In order to understand the spatial distribution of the two populations in Terzan 5, I computed the projected number density profile of the cluster by using direct star counts on the retrieved catalogs. First of all, I needed to calculate the

center of the cluster. The center of mass is defined as:

$$x_{CM} = \frac{\sum_{i=1}^{N}(x_i \times m_i)}{\sum m_i} \quad y_{CM} = \frac{\sum_{i=1}^{N}(y_i \times m_i)}{\sum m_i} \quad z_{CM} = \frac{\sum_{i=1}^{N}(z_i \times m_i)}{\sum m_i} \tag{3.4}$$

where x_i, y_i, z_i are the positions of the particles in the cluster and m_i their masses. Assuming an equivalent unitary mass for all the stars, which for an old globular cluster is acceptable, I calculated the coordinates of the cluster's center of density using the shrinking sphere technique, which makes use of the calculation of the center of mass. At each step, the center of mass is calculated and the radius of the sphere that surrounds it is reduced, identifying the point of greatest density of the cluster, that is the real center. I defined the number density by simply counting objects for each radial distance bin.
This calculation was done for the two populations separately. Figure 3.11 shows the density profile for the metal poorer (in blue) and metal richer (in red) populations. The MP appears to be less concentrated towards the center and more spread in the outer part of the cluster with respect to the MR, which is more concentrated and reaches a density at the center $\rho > 1$ arcsec^{-2}). These results are consistent with the ones from Lanzoni et al. 2010. In Table 3.1 the CM (Center of Mass) for the entire cluster and for the two populations separately is reported.

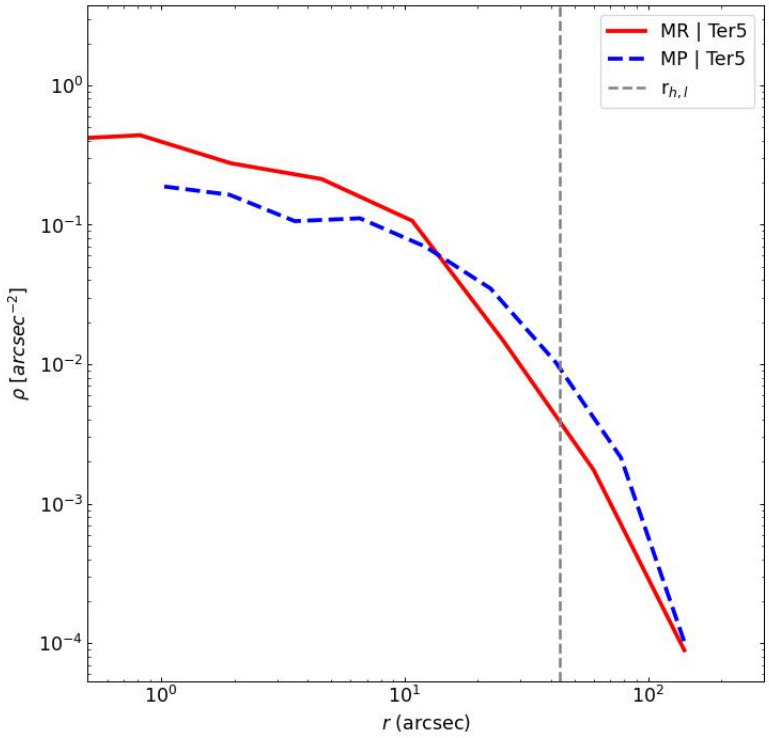

Figure 3.11: Density profile of the stars in Terzan 5 with respect to the distance from the center in arcseconds. The blue line corresponds to the MP population, and the red line to the MR.

I then computed the density maps of the two populations separately, plotted in

Table 3.1: Center of mass for the entire Terzan 5 cluster and the two populations separately. MP in the MP population, MR in the MR. The grey dotted line highlights the half-light radius for the cluster.

	CM_{tot}	CM_{MP}	CM_{MR}
x_{CM} [arcsec]	221.576	224.568	221.104
y_{CM} [arcsec]	222.880	223.732	223.192
x_{CM} [deg]	0.0615	0.0624	0.0614
y_{CM} [deg]	0.0619	0.0621	0.0620

Figure 3.12. The quantities on the abscissa and ordinate are the projected 2D stellar coordinates relative to the cluster center. The color levels are indicative of the stellar density and are based on the 2D binned density estimate by defining a grid of bins within which the number of enclosed stars was measured, to define the contour lines. The color bar is given in logarithmic scale. The MR population (right panel in Figure 3.12) appears more concentrated towards the center and denser towards almost the entire analyzed field of view.

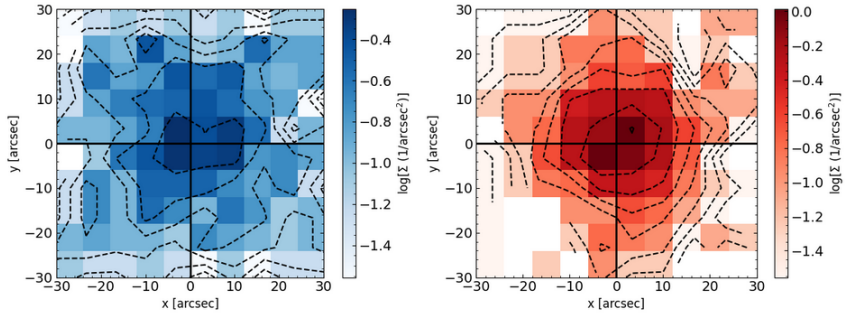

Figure 3.12: Density maps of the MP (left panel) and MR (right panel) populations in Terzan 5.

3.5 Internal kinematics

The obtained measurements allowed me to investigate the internal dynamics of Terzan 5. For the first time for this cluster, I analyzed the average internal motions of stars in MP and MR populations separately as a function of the radial distance from the cluster center, with the aim to check for any signs of rotation within the cluster and for any sign of anisotropy between the radial and tangential motions for both the populations.

3.5.1 Rotation in the plane of the sky

As a first step, I converted the $\mu_\alpha cos\delta$ and μ_δ components of PMs into a motion in polar coordinates on the plane of the sky and with origin the center of the cluster, with positive μ_r indicating velocities away from the cluster center and positive μ_t indicating counterclockwise movements (Bianchini et al. 2018). I then exploited a Supermongo pipeline to bin each population in such a way

as to have the same number of stars in each bin. The total number of bins is 8, chosen as a compromise not to have too much noise and not to have a too low number of bins. Finally, I estimated the uncertainty relative to each point by bootstrapping with replacements, a procedure which was performed 1000 times and results in the error bars plotted over the points.

The radial and tangential motions versus the distance from the cluster center are shown in Figure 3.13. The radial coordinate has been normalized to the half-light radius $r_{h,l} = 0.012$ deg from W.E. Harris 1996 (2010 edition) database. The grey dotted line highlights the distance beyond which $r > r_{h,l}$.

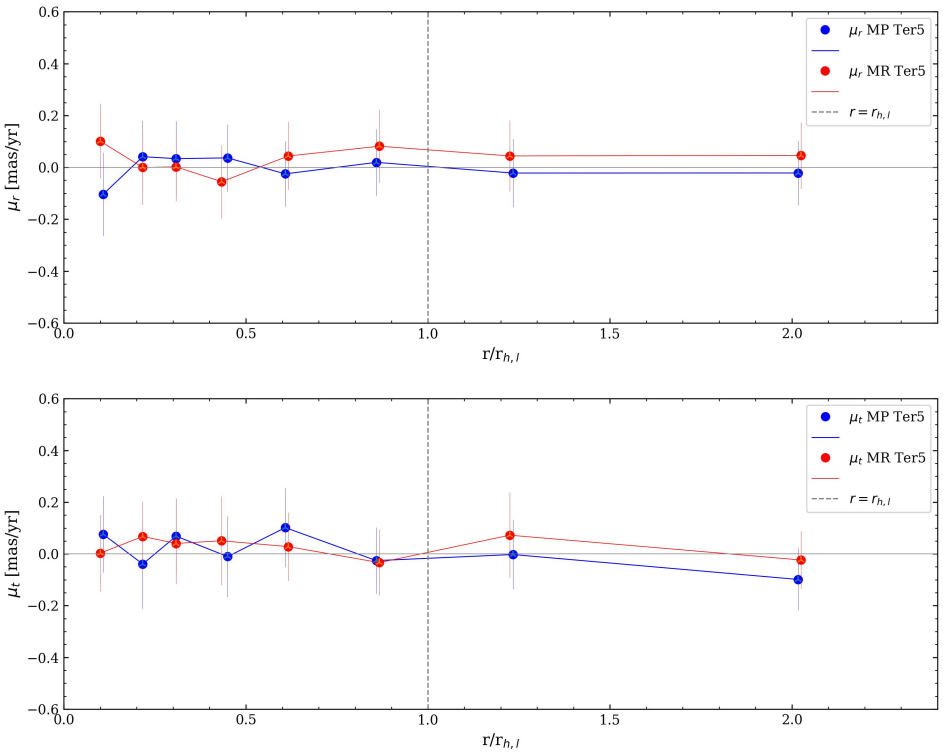

Figure 3.13: Average radial (upper panel) and tangential (lower panel) profile as a function of the radial distance from the cluster center. The radial quantity is normalized over the half-light radius from W.E. Harris 1996 (2010 edition) database. The grey dotted line highlights $\frac{r}{r_{h,l}} = 1$.

A visual inspection of Figure 3.13 suggests that both the radial and tangential profiles of the two populations are consistent with zero motion. This is due to the presence of high statistical noise caused by the binning procedure, which determines error bars that are largely from the bootstrapping procedure. The motions reach a maximum amplitude of about 0.18 mas/yr at a radial distance of around 0.1 half-light radii, but the error bars are consistent with 0 mas/yr. These results seem not to be enough to witness consistency with both a radial and tangential global rotation for the two populations in Terzan 5. However, it does witness the consistency and similarity of the radial and tangential motion for both the MP and MR populations, within 1σ.

3.5.2 Velocity dispersion profiles

To calculate the radial and tangential velocity dispersion (σ_r and σ_t) as a function of distance from the cluster center, I followed the procedure described in Mackey et al. 2013, Marino et al. 2014 and Bianchini et al. 2018. It briefly consists in maximizing the likelihood function:

$$\lambda = \Pi_{i=1}^{N} p(v_i, \epsilon_i)$$

with the probability of finding a star with velocity v_i and uncertainty ϵ_i defined by:

$$p(v_i, \epsilon_i) = \frac{1}{2\pi\sqrt{(\sigma^2 + \epsilon_i^2)}} exp(-\frac{(v_i - v)^2}{2(\sigma^2 + \epsilon_i^2)}) \tag{3.5}$$

This was done following a Supermongo pipeline written by J. Anderson and modified by A. Milone. To determine 1σ uncertainties I calculated the parameter limits for the region containing the central 68.3% of the likelihood distribution function. I then re-computed them by bootstrapping with the replacement 1000 times. These are the ones shown in the velocity dispersion profiles as a function of the radial distance represented in Figure 3.14. As before, the radial coordinate was normalized to the half-light radius $r_{h,l}$ from W.E. Harris 1996 (2010 edition) database.

The velocity dispersions of both the MP and MR populations in Terzan 5 reach their maximum values at around 0.45 mas/yr in the innermost analyzed region, and decline in the cluster outskirt. σ_t overall trend seems a bit higher than σ_r for $r < r_{h,l}$, but it is highly affected by the statistical noise due to the binning. There are no other significant differences between the radial and tangential dispersions to be highlighted. The only justifiable conclusion is that within 0.30 and 0.45 mas/yr the dispersion seems to be overall constant.

3.5.3 Anisotropy

To further explore these findings, I computed the radial dependence of the deviation from isotropy of each population. I quantified the anisotropy as $\beta = \frac{\sigma_t}{\sigma_r} - 1$ (in agreement with what done for example by Cordoni et al. 2020 and Bellini et al. 2015), with $\beta < 0$ indicating radial anisotropy and $\beta > 0$ tangential anisotropy. $\beta = 0$ or compatible with zero is characteristic of an isotropic stellar system.
The anisotropy parameter β for the populations of Terzan 5 is plotted as a function of the radial distance from the cluster center in Figure 3.15. The radial coordinate is normalized to the half-light radius $r_{h,l}$ from W.E. Harris 1996 (2010 edition) database.

The results show that the studied populations in Terzan 5 are both radially and tangentially isotropic in both the central and external regions of the cluster. Even if a small tangential anisotropy seems to be present, with β reaching

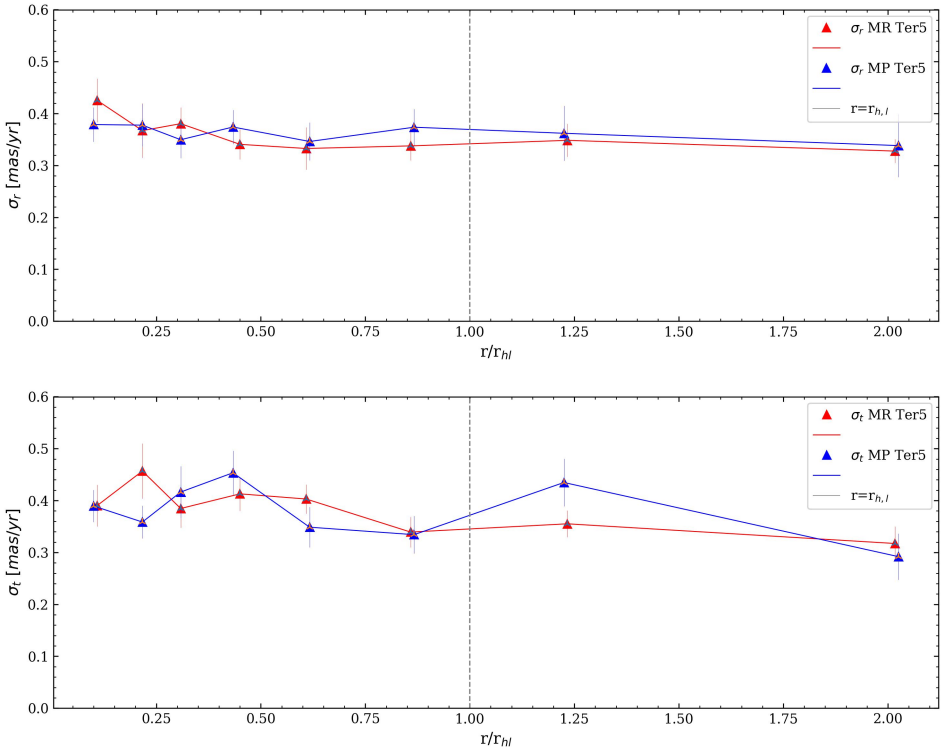

Figure 3.14: Average radial (upper panel) and tangential (lower panel) velocity dispersions profile as a function of the radial distance from the cluster center. The radial quantity is normalized over the half-light radius from W.E. Harris 1996 (2010 edition) database. The grey dotted line highlights $\frac{r}{r_{h,l}} = 1$.

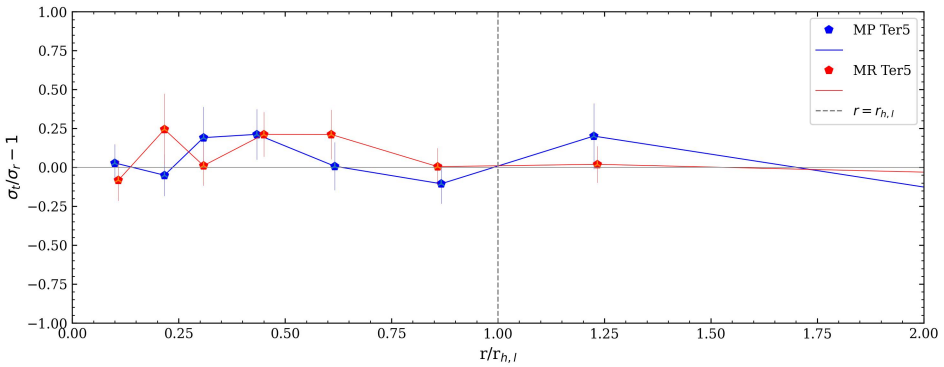

Figure 3.15: Anisotropy parameter β showing the deviation of isotropy for the MP (in blue) and MR (in red) populations in Terzan 5. The radial quantity is normalized over the half-light radius from W.E. Harris 1996 (2010 edition) database. The grey dotted line highlights $\frac{r}{r_{h,l}} = 1$.

positive values of 0.25 and thus suggesting that the MP population populates the cluster preferentially on tangential orbits, it is consistent with zero within the error bars. We could say that in the innermost region probed by HST observational data the difference in the radial and tangential motion for both

the MP and MR populations is stronger (their behavior seems to be somehow mirrored) than for $r > r_{h,l}$, were within the errors, both the populations are consistent with an isotropic system. However, taking into account the statistical noise, the tangential and radial profiles are consistent with isotropy in the entire considered radial distance.

Chapter 4

Numerical evolutionary models of a Terzan 5-like cluster

In this Chapter, I present the N-Body simulations that I did by using `NBSymple` in collaboration with the GEPI Department at the Observatoire de Paris-Meudon during my Erasmus Traineeship. The Chapter is organized as follows. Section 4.1 describes (without going into details) the main features of the N-body problem. Section 4.2 briefly explains how the code `NBSymple` works. Section 4.3 shows how the initial conditions of our numerical models are given to the code starting from a King profile. Section 4.4 presents the results of three different models with their respective analyses and comparison with Terzan 5 observative results.

4.1 N-body problem

In a system of N gravitating point-masses, the force of the ith body of mass m_i and position vector $\vec{r}_i$ in a Cartesian reference frame is the sum of the individual forces $\vec{F_{ij}}$ due to all the other $j = 1, 2, ..., N$, $j \neq 1$, bodies as given by:

$$\vec{F_{ij}} = G\frac{m_i m_j}{|\vec{r}_j - \vec{r}_i|^3}(\vec{r}_j - \vec{r}_i) \tag{4.1}$$

such that the total force acting on i, $\vec{F}_i$ is:

$$\vec{F}_i = \sum_{j=1, j\neq i}^{N} \vec{F}_{ij} = Gm_i \sum_{j=1, j\neq i}^{N} \frac{m_j}{|\vec{r}_{ij}|^3}\vec{r}_{ij} \tag{4.2}$$

where we set $\vec{r}_{ij} = \vec{r}_j - \vec{r}_i$. The anti-symmetry condition $\vec{F}_{ij} = -\vec{F}_{ji}$ holds, implying the linear and angular momentum conservation laws for the isolated case. The resulting system of equations of motion, subjected to given initial conditions, is:

$$\begin{cases} m_i \ddot{\vec{r}}_i = \vec{F}_i + \vec{F}_{ext}(\vec{r}_i) \\ \vec{r}_i(0) = \vec{r}_{i0} \\ \dot{\vec{r}}_i(0) = \vec{r}_{i0} \end{cases} \tag{4.3}$$

where $\vec{F}_{ext}$ accounts for an external force, expressed by $\vec{F}_{ext}(\vec{r}_i) = \nabla U_{ext}(\vec{r}_i)$ if conservative (∇ is the usual gradient operator acting on the external force potential U_{ext}).
There is no general analytic solution to the N-body problem for $N \geq 3$, so numerical methods must be used. Implementation of such methods is challenging due to the co-existence of problems on both small scales, as close gravitational encounters, and large ones, as the fact that the Newtonian pair-wise gravitational force never vanishes, so that every component of the system, however distant, contributes to the force calculation. This 'double divergence' of the classic Newtonian interaction potential has two different consequences:

- problem (i): close encounters correspond to an unbound force between colliding bodies, which means that $|\vec{F}_{ij}| \to \infty$ when $|\vec{r}_{ij}| \to 0$, yielding to an unbound error in the relative acceleration;
- problem (ii): the need of the force summation over the whole set of distinct $N(N-1)/2$ pairs in the system implies an overwhelming CPU challenge for values of N of astrophysical interest over a sufficient number of time steps, practically unaffordable even with most modern, fast CPUs.

Actually, the number of floating point operations for the force evaluation among $N = 1000$ stars (galactic open cluster) is about 12.5 million, rising to 125 billion for an $N = 10^5$ star system (a modest globular cluster) requiring a time of the order of 0.00125 and 12.5 s, respectively, to a single multi-core processor working at 10 GFlop/s speed. A full view of system evolution will require covering about 3000 and $2{\times}10^5$ crossing times, respectively. Considering a minimum of 1000 time steps per crossing time, this corresponds, in the case $N = 1000$, to $\sim$1 h of simulation just to evaluate forces and without considering the additional $O(N)$ computations time required by time integration. The computation time grows to an unaffordable 84 years time for $N = 10^5$ (Capuzzo-Dolcetta et al. 2011).
Problem (i) is often cured by introducing a softening parameter ϵ in the interaction potential, which assumes a smoothed form:

$$U_{ij} = G\frac{m_j}{\sqrt{(|\vec{r}_{ij}|^2 + \epsilon^2)^{3/2}}} \tag{4.4}$$

The corresponding total force acting on the ith particle is:

$$\vec{F}_i \sim Gm_i \sum_{j=1}^{N} \frac{m_j \vec{r}_{ij}}{(|\vec{r}_{ij}|^2 + \epsilon^2)^{3/2}} \tag{4.5}$$

In the latter sum, the condition $j \neq i$ is no longer needed, because in its smoothed form, $\vec{F}_{ij} = 0$ if $\epsilon \neq 0$. The introduction of the softening parameter corresponds to substitute point masses with Plummer's spheres (Plummer, 1911) where the mass m_i is distributed around the center according to the density law:

$$\rho_i(r) = \frac{3m_i}{4\pi} \frac{\epsilon^2}{(\epsilon^2 + r^2)^{5/2}} \tag{4.6}$$

In this work, the softened interaction was used, by means of a softening parameter $\epsilon = (\frac{4}{3}\frac{\pi r_h^3}{N/2})^{\frac{1}{3}}$, corresponding to the average inter-particle distance by the half-mass radius.

Problem (ii) is faced in different ways. The common line consists in introducing averaging methods (called "main-field") dividing the force acting on a particle and due to the rest of the system into a "large" scale, slowly varying, coarse-grain, contribution $\vec{F}_{is}$, and into a "small" scale, rapidly varying, fine-grain, contribution represented as a summation limited to a set of $n < N$ neighboring particles, to give:

$$\vec{F}_i \sim G m_i \sum_{j=1}^{n} \frac{m_j \vec{r}_{ij}}{(|\vec{r}_{ij}|^2 + \epsilon^2)^{3/2}} + \vec{F}_{is}(\vec{r}_i) \tag{4.7}$$

The direct summation is usually performed considering an individual value of n as that given by the number of neighbor stars, as those contained in a sphere of radius such to guarantee a sufficient resolution of the granular component of the field, while farther stars give the large scale force $\vec{F}_{is}$ which can be evaluated in different ways. Of course, setting $n = N$ (if the neighbouring sphere contains all the system particles) makes the approximated expression above equal to the correct direct summation; in this case, $\vec{F}_{is}$ is contributed by an external force, only, and thus corresponds to $\vec{F}_{ext}$ in Equation 4.3.

4.2 The code: `NBSymple`

In this work I used an improved version of `NBSymple`, a code conceived to be a high precision, fast and reliable code to study the evolution of gravitational N-body systems (Capuzzo-Dolcetta, Mastrobuono-Battisti et al. 2011), to be applied to the study of systems composed by a number of objects up to few million, covering the astrophysical range from planetary systems ($N \leq 10^6$) to stellar systems of the size of open clusters and globular clusters ($N \sim 10^6$). The new version of `NBSymple` we used includes a stellar evolution and a star formation module (Lacchin et al. in prep) and, therefore, it is perfectly suited to study the formation and evolution of GCs with multiple stellar populations, such as Terzan 5. The aims of high precision and fast code to simulate non-isolated self-gravitating N-body systems of astrophysical interest are approached to (i) direct summation (to avoid truncation error in force evaluation), that is setting $n = N$ in Equation 4.7, and (ii) the use of high order, symplectic

time integration methods. With `NBSymple` the speed is attained by implementing direct summation codes on a hybrid architecture where multicore CPUs are linked to Graphic Processing Units (GPUs) acting as computational accelerators. The code can form multiple populations at different times, depending on the model adopted, with assumed star formation rates, so that all stars in the second population form in a decided time interval depending on the theoretical models.

4.3 Methods and analysis outline

The improved version of `NBSymple` (Capuzzo-Dolcetta et al. 2011) takes as input the initial conditions from an external file for the N particles of the system, whose individual masses, for simplicity, are chosen to have all the same value if they are within the same stellar population. The units are fixed to 10 pc for the positions, $10^5 M_\odot$ for the masses and 6.559 km/s for the velocity components. The assumption $G = 1$ in the equations of motion is made, implying that the 'crossing' time $T = (GM)^{-1/2} R^{3/2}$ is the unit of time. The forces due to the mutual interaction among stars in the cluster (internal forces) are given by Equation 4.5 and the external force is then added. For the external force, the Galactic model consists of a dark-matter halo and both a thin and a thick disc. The functional forms of these components are taken from Allen & Santillan 1991 while the relative parameters are given by Pouliasis et al. 2017, Model II, as explained in Mastrobuobo-Battisti et al. 2019.
Ordinary numerical methods for integrating Newtonian equations of motions become dissipative and exhibit incorrect long-term behavior. One possible solution is using symplectic integrators. A symplectic transformation is such that the two-form $dp \wedge dq$ is conserved exactly, so that $(q(0), p(0)) \to (q(s), p(s))$ is a canonical transformation (q and p are vectors of conjugate coordinates). Symplectic integrations may have problems in following the evolution of chaotic systems, but these problems are much smaller than with non-symplectic methods. The choice of symplectic methods is wide, for it is possible the construction of high order integrators (Yoshida 1991). `NBSymple` allows the choice of two different symplectic methods. The one used in this work is the simple *leapfrog* method, which is second-order accurate.

4.3.1 Initial conditions

The most commonly used models to describe spherically symmetric systems are King models. These models can well fit the brightness distributions of globular clusters and some elliptical galaxies, and are based on the following distribution function:

$$f_K(\epsilon) = \begin{cases} \rho_1 (2\pi\sigma^2)^{-3/2} (e^{\epsilon/\sigma^2} - 1) & \epsilon > 0 \\ 0 & \epsilon < 0 \end{cases} \tag{4.8}$$

where ϵ is the relative energy $\epsilon = -E + \Phi_0 = \Psi - v^2/2$ and Ψ is the relative potential $\Psi = -\Phi + \Phi_0$. This distribution function may be viewed as a trun-

cated isothermal sphere. The characteristic of this model is that the relative potential Ψ and density of stars ρ in the mass distribution become equal to zero at some finite radius r_t, the tidal radius. The value of r_t depends on the central potential $\Psi(0)/\sigma^2$ and King radius defined as $r_0 = \sqrt{9\sigma^2/4\pi G\rho_0}$. In the limit $\Psi(0)/\sigma^2 \to \infty$ the isothermal sphere is recovered and r_t extends to infinity.
The King models are parametrized by the central potential $W_0 = \Psi(0)/\sigma^2$ or the concentration $c = log_{10}(r_t/r_0)$. In these models, the tidal radius or c is uniquely determined by the value of the central potential W_0. The greater the value of the central potential, the greater the tidal radius.

In our models, we have considered that the stars all have the same mass and isotropic velocity distribution. Of course, these models represent the simplest version and can be extended to include a mass spectrum, velocity anisotropies, and rotation, as seen in many observed clusters.
After setting the initial conditions from the King model, the orbit of the cluster was integrated backward in time for 12 Gyr to find the original position of the cluster, and to be able to start the simulation forward in time from there. In the backward integration, we used a point mass cluster moving in the same Galactic potential as adopted for the N-body system that we then simulated forward in time for 12 Gyr.

The initial conditions of the King model for the two populations that we simulated, called First Generation (FG, related to MP in Terzan 5 real cluster) and Second Generation (SG, related to MR in Terzan 5), of the three models presented in this work, are listed in Table 4.1 and 4.2. W_0 is the central value of the rescaled gravitational potential $V(r)$, such that every integration of Poisson's equation leads to a valid King model. The larger the value of W_0, the larger is the surface radius; as $W_0 \to \infty$, the velocity distribution approaches Maxwellian, the surface radius increases without limit, and the model approaches the isothermal sphere. In our models, we used an FG with $W_0 = 5$ while $W_0 = 8$ for the SG, choosing the first one less dense than the second because today we observe the SG more concentrated than the FG. r_t and r_h are respectively the tidal radius and the half-mass radius of the cluster. r_0 is the core radius of the cluster.

The initial mass is also based on what we observed today, so we expect the former, being more extended, to lose more mass than the latter. This is why in the initial conditions the total mass of the FG is equal to $3.57 \times 10^6 M_\odot$ and of the SG is $7.5 \times 10^5 M_\odot$.

Table 4.1: Initial conditions of the King model for the FG in model 1.

W_0	M_{tot} [$M_\odot$]	r_0 [pc]	r_t [pc]	r_h [pc]
5	3.57 $\times 10^6$	9.35	100	18.7

Table 4.2: Initial conditions of the King model for the SG in model 1.

W_0	M_{tot} [$M_\odot$]	r_0 [pc]	r_t [pc]	r_h [pc]
8	7.5 $\times 10^5$	0.274	18.7	1.95

4.3.2 Analysis outline

After retrieving the final evolutionary snapshot of the model, I analyzed the results of the simulation. For each model, the applied analysis pipeline is the same and is analogous to the one made on the data from HST in order to allow a direct comparison between the data and the models. The applied analysis steps are the following.

- Calculation of the coordinates of the cluster's center of density using the shrinking sphere technique, which passes through the calculation of the center of mass. At each step, the center of mass is calculated and the radius of the sphere that surrounds it is reduced, identifying the point of greatest density of the cluster, that is the real center. The center of mass is defined as

$$x_{CM} = \frac{\sum_{i=1}^{N}(x_i \times m_i)}{\sum m_i} \quad y_{CM} = \frac{\sum_{i=1}^{N}(y_i \times m_i)}{\sum m_i} \quad z_{CM} = \frac{\sum_{i=1}^{N}(z_i \times m_i)}{\sum m_i} \tag{4.9}$$

  where x_i, y_i, z_i are the positions of the particles in the cluster and m_i their masses;

- Calculation of the energy E_i of each ith particle defined as

$$E_i = \frac{1}{2} m_i v_i^2 - m_i \times \sum_{i=1}^{N} \frac{M}{r_i} \tag{4.10}$$

  with $v_i = \sqrt{(v_{x,i} - v_{x_{CM},i})^2 + (vyi - v_{y_{CM},i})^2 + (v_{zi} - v_{z_{CM},i})^2}$ and v_x, v_y, v_z the velocity components (calculated starting from the velocity of stars belonging to the shrinking sphere), $r_i = \sqrt{(x_i - x_{CM})^2 + (y_i - y_{CM})^2 + (z_i - z_{CM})^2}$ and M is the total mass;

- Selection of the bound particles, which are the ones with negative energy $E < 0$ with respect to the other cluster members;

- Conversion into celestial coordinates obtaining *R.A.*, DEC and components of the PMs;

- Separate analysis of the two different populations: one first generation of the Terzan 5-like GC, corresponding to the metal poorer and older population in Terzan 5; one-second generation, corresponding to the metal richer and younger (and more concentrated) population in Terzan 5;

- Calculation of the density of the two populations separately as described in Section 3.4;

- Production of the isodensity plots on xy, xz, and yz planes, as described in Section 3.4;

- Analysis of the positions in equatorial and celestial coordinates;
- Analysis of the PMs of the two populations separately and of the entire final cluster;
- Calculation of the half-mass radius $r_{h,m}$ of the cluster and of the two stellar populations separately; plots of the PMs as a function of the distance r from the cluster center with the half-mass radius highlighted as a vertical line;
- Projection of the motions in celestial coordinates into the radial and tangential direction; calculation of the velocity dispersions and plots of the dispersions as a function of r normalized to the half-mass radius;
- Calculation of the anisotropy parameter as described in Section 3.5 and plots of the anisotropy as a function of r normalized to the half-mass radius.

4.4 Results

4.4.1 Model 1: scenario I

In this first model, the SG is born from the gas left by the supernova explosions of the FG, after 7.5 Gyr. The SG forms in 60 Myr, with a constant star formation rate throughout this time interval. At the end of the simulation, the FG has 12 Gyr and the SG has 4.5 Gyr. This corresponds to the Scenario I described in Section 1.3.1. The initial conditions are listed in Table 4.1 and 4.2.

I analyzed the final snapshot obtained from the simulation, which corresponds to the current state of the cluster. In Table 4.3 total mass and the mass of the first and second population of the cluster (considering just bound stars) are given. $M_{tot,f}$ is the final mass of the particles which in the final snapshot are still bound to the cluster; M_{FG} is the fraction of the final mass belonging to the FG; M_{SG} is the fraction of the final mass belonging to the SG. We see the FG is the 61% of the total mass of the cluster. This is consistent with Terzan 5. The total mass is not equal, but compatible in order of magnitude with Terzan 5's mass $(9.35 \pm 0.69) \times 10^5$ (Baumgardt et al. 2021).

Table 4.3: Mass values in the final snapshot after 12 Gyr of the Terzan 5-like cluster in model 1.

$M_{tot,f}$ $[M_\odot]$	M_{FG} $[M_\odot]$	M_{SG} $[M_\odot]$
1.21×10^6	7.81×10^5	4.94×10^5

The center of density, calculated as explained in Section 4.3.3, is slightly different for the entire Terzan 5-like cluster and the two populations separately. The centers of density of the two populations and for the entire cluster are given in Table 4.4. The distance in parsec between the center of mass of the MP and of the MR populations is 0.11 pc, which corresponds to the 2% of the total half-mass radius for this cluster.

Table 4.4: Center of mass for the entire Terzan 5-like cluster and the two populations separately in model 1. FG is the first generation stellar population, corresponding to MP in Terzan 5, while SG is the second generation, corresponding to MR.

	CM_{tot}	CM_{FG}	CM_{SG}
x_{CM} [pc]	841.52	841.56	841.46
y_{CM} [pc]	1593.42	1593.41	1593.45
z_{CM} [pc]	152.21	152.22	152.19
$v_{x_{CM}}$ [km/s]	52.55	52.55	52,54
$v_{y_{CM}}$ [km/s]	-2.00	-1.98	-2.03
$v_{z_{CM}}$ [km/s]	-25.73	-25.69	-25.79

The position of the cluster in the Galaxy at the end of the simulation (running from 0 up to 12 Gyr) is shown in Figure 4.1. The blue particles are the ones still bound to the cluster.

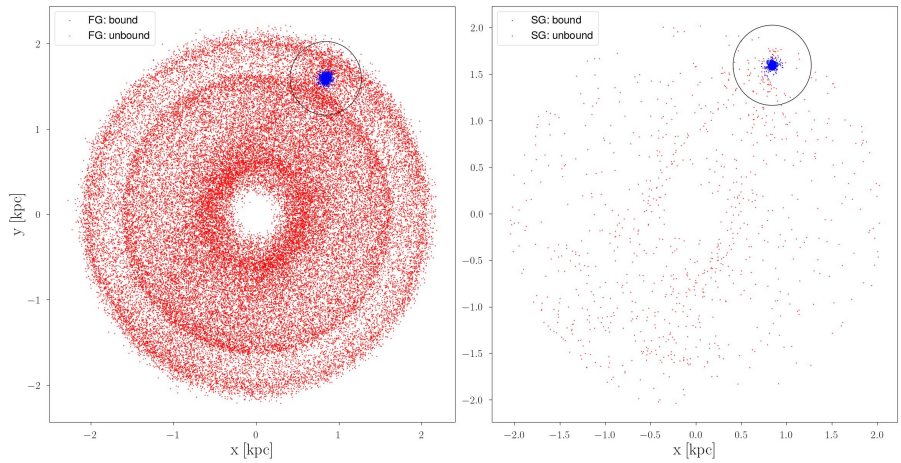

Figure 4.1: Motion of Terzan 5-like cluster around the Galaxy for the first model, reproducing scenario I. In blue the bound particles are shown. The black circle highlights the distance of the most distant bound star belonging to the cluster. FG (left panel) is the first generation, corresponding to MP in Terzan 5, while SG (right panel) is the second generation or MR in Terzan 5.

The bound particles were used to compute the density of the Terzan 5-like cluster, analogously to what was done in Section 3.4 for Terzan 5. The result is shown in Figure 4.2.

The density maps of the two populations separately were plotted analogously to Terzan 5 in Section 3.4. On the abscissa and ordinate, there are the projected 2D stellar coordinates relative to the cluster center. The color levels are indicative of the stellar density, based on the 2D binned density estimated by defining a grid of bins within which the number of enclosed stars was calculated, to define the contour lines. The color bar is given in logarithmic scale. The maps on the xy plane for FG (MP for Terzan 5) and SG (MR for Terzan 5) are shown in Figure 4.3.

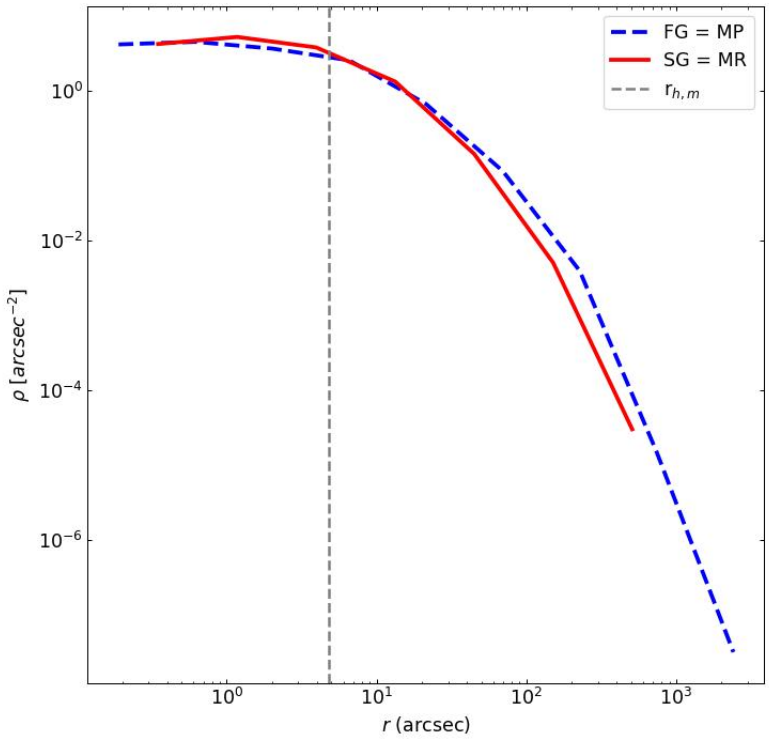

Figure 4.2: Density profile of the stars in the first model Terzan 5-like cluster with respect to the distance from the center in arcseconds. The blue line corresponds to the FG (MP in Terzan 5), the red line to the SG (MR in Terzan 5). The grey dotted line highlights the logarithmic value of the total half-mass radius of the cluster in arcseconds.

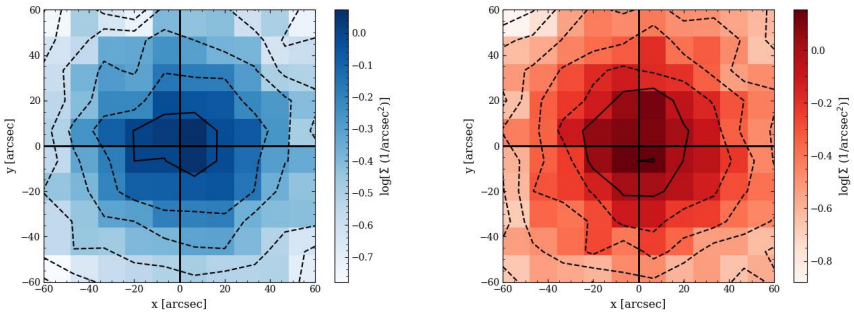

Figure 4.3: Density maps of the FG (left panel) SG (right panel) populations in the first model Terzan 5-like cluster, on the xy plane.

From the density profiles and density maps we see that the SG is denser than the FG for $1 < r < 10$ arcsec, which corresponds to $r \lesssim 0.5$ pc, the very center of the cluster. Moreover, as the maps show, the SG appears to be more concentrated towards the center. This peculiarity in the density of the particles for this Terzan 5-like cluster is well within the half-mass radius, which was calculated for the entire Terzan 5-like cluster and for the two populations separately. The results are listed in Table 4.5.

The obtained measurements allowed me to investigate the internal dynamics

Table 4.5: Half-mass radius for the entire Terzan 5-like cluster, the FG (MP in Terzan 5) and the SG (MR in Terzan 5) separately.

	$r_{h,tot}$	$r_{h,FG}$	$r_{h,SG}$
[deg]	0.035	0.044	0.025
[pc]	5.459	6.932	3.934

of the Terzan 5-like cluster, such as I did for Terzan 5 and described in Section 3.5. Before doing this, I computed the proper motions along the Right Ascension and Declination directions, $\mu_\alpha cos\delta$ and μ_δ, using the astropy conversion package from the Cartesian coordinates and velocities provided by the simulation output. This is shown in Figure 4.4.

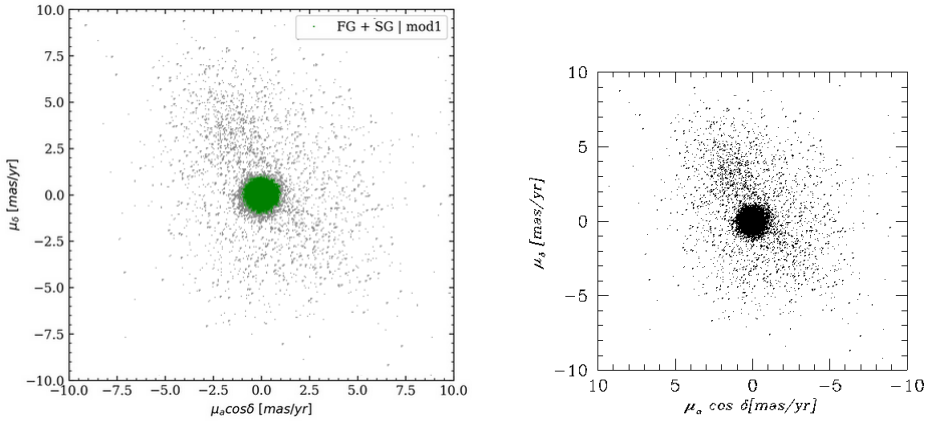

Figure 4.4: Proper motion distributions for the first Terzan 5-like cluster along the RA and DEC directions, with Terzan 5 observational results in grey in the background. To use as a comparison, on the left panel we see the proper motions for Terzan 5 cluster.

I then analyzed the average internal motions of stars in the FG (corresponding to MP in Terzan 5) and SG (or MR) populations separately as a function of the radial distance from the cluster center, with the aim to check for any signs of rotation within the cluster and for any sign of anisotropy between the radial and tangential motions for both the populations.

As a first step, I converted the $\mu_\alpha cos\delta$ and μ_δ components of PMs into a radial (μ_r) and a tangential (μ_t) motion on the plane of the sky. To do so, I used a Python code exploiting *astropy* package. Further on, I calculated the radial and tangential velocity dispersion (σ_r and σ_t) as a function of distance from the cluster center with a Python code implementing the same identical reasoning done in Section 3.5.2 using Supermongo. The obtained velocity dispersion profiles for this model are represented in Figure 4.5.

The velocity dispersions of both the FG-MP and SG-MR populations in Terzan 5-like cluster reach their maximum values at around 0.3 km/s in the innermost analyzed region, a lower value with respect to Terzan 5, and decline in the modeled cluster outskirts, as for the real cluster. However, even if σ_t results more affected by noise, its overall trend seems a bit higher than σ_r for $r < r_{h,tot}$.

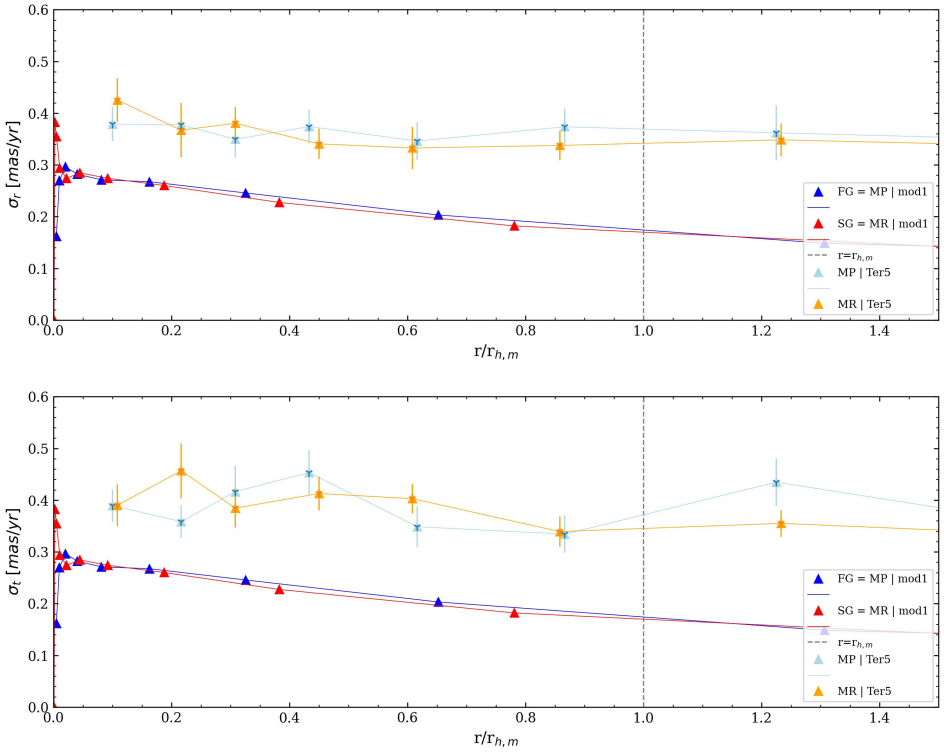

Figure 4.5: Average radial (upper panel) and tangential (lower panel) velocity dispersion profile as a function of the radial distance from the Terzan 5-like cluster center, in the first model. The radial quantity is normalized over the total half-mass radius equal to 0.035 deg. The grey dotted line highlights $\frac{r}{r_{h,tot}} = 1$. The observational results are shown too: MP population in light blue, MR in orange. They are normalized to the half-light radius of Terzan 5, $r_{h,l}$=0.012 deg.

This is consistent with the observational results.

I then quantified the radial dependence of the deviation from isotropy of each population, using the parameter β describing anisotropy as explained in Section 3.5.3. The anisotropy parameter for the populations of the first model Terzan 5-like cluster is plotted as a function of the radial distance from the cluster center in Figure 4.6. The radial coordinate is normalized to the half-mass radius $r_{h,tot}$ (see Table 4.5).

The results show that the studied populations in Terzan 5-like cluster are consistent with isotropy in both the central and external regions of the cluster, except for some spikes near the very center caused by the limited resolution of the model. The comparison between the results from this model and the observations are shown in Figure 4.7.

The first model Terzan 5-like cluster is consistent with zero anisotropy such as Terzan 5 real cluster. The general trend of the modeled data points seems slightly different from the observational data because the former is not affected by the noise, while the latter are. The deviations from isotropy (an apparent very small tangential anisotropy for the FG-MP population, as in Terzan 5,

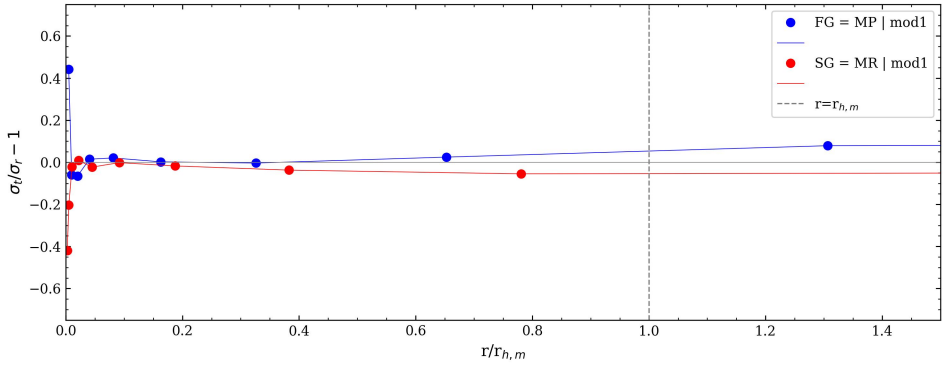

Figure 4.6: Anisotropy parameter β showing the deviation of isotropy for the MP (in blue) and MR (in red) populations in first model Terzan 5-like cluster. The radial quantity is normalized over the half-mass radius equal to 0.035 deg. The grey dotted line highlights $\frac{r}{r_{h,tot}} = 1$.

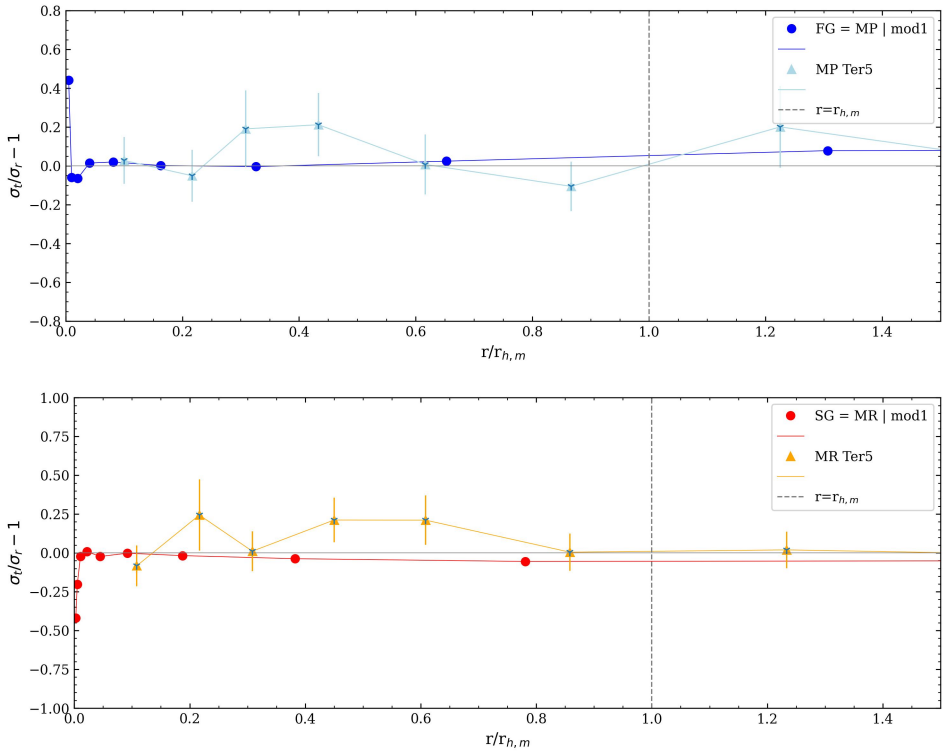

Figure 4.7: Anisotropy parameter β showing the deviation of isotropy for the MP (in blue) and MR (in red) populations in the first model Terzan 5-like cluster. In the upper panel, the cluster-like results are compared with the observed ones for the FG-MP population, in the lower panel the same is done with the SG-MR population. The radial quantity is normalized over the half-mass radius equal to 0.035 deg. The grey dotted line highlights $\frac{r}{r_{h,tot}} = 1$.

and very small radial anisotropy for the SG-MR population, unlike the observational counterpart) are minimal. More details are given in Section 5.

4.4.2 Model 2: scenario II

In the second model of a Terzan 5-like cluster, the FG and SG are almost the same age and are born with a temporal difference of ~ 40 Myr. The SG forms within 40 and 100 Myr with a constant star formation rate. This corresponds to Scenario II described in Section 1.3.2. The initial conditions of the King model for the FG and SG are identical to the ones of the first model.

I analyzed the last snapshot of the simulation, as in the previous model. In Table 4.6 the masses of the cluster, the FG, and SG (considering just bound stars) are given. The meaning of the parameters is the same as described in Section 4.4.1. We see the FG is 70 % of the total mass of the cluster. This is a higher percentage with respect to what was obtained from the first model, but still consistent with the Terzan 5 real cluster. The total mass, moreover, is in the range of Terzan 5's mass as given by Baumgardt et al. 2021 and Harris 1996 (2010 edition).

Table 4.6: Mass values in the final snapshot after 12 Gyr of the Terzan 5-like cluster in model 1. In the order of presentation: $M_{tot,f}$ is the final mass of the particles which in the final snapshot are still bound to the cluster; M_{FG} is the fraction of the final mass belonging to the FG; M_{SG} is the fraction of the final mass belonging to the SG.

$M_{tot,f}$ $[M_\odot]$	M_{FG} $[M_\odot]$	M_{SG} $[M_\odot]$
1.48×10^6	1.03×10^6	4.46×10^5

The center of mass, calculated as explained in Section 4.3.3, is slightly different for the entire Terzan 5-like cluster and the two populations separately, such as in the previously presented model. The different centers are given in Table 4.7. The distance in parsec between the center of mass of the MP and of the MR populations is 0.14 pc, corresponding to the 2% of the total half-mass radius.

Table 4.7: Center of mass for the entire Terzan 5-like cluster and the two populations separately in model 1. FG is the first generation stellar population, corresponding to MP in Terzan 5, while SG is the second generation, corresponding to MR.

	CM_{tot}	CM_{FG}	CM_{SG}
x_{CM} [pc]	-481.72	-481.72	-481.73
y_{CM} [pc]	-1281.97,	-1281.93	-1282.05
z_{CM} [pc]	-193.59	-193.61	-193.54
$v_{x_{CM}}$ [km/s]	-95.65	-95.63	-95.70
$v_{y_{CM}}$ [km/s]	-74.92	-74.90	-74.97
$v_{z_{CM}}$ [km/s]	-17.23	-17.23	-17.23

The position of the cluster in the Galaxy at the end of the simulation (running from 0 up to 12 Gyr) is shown in Figure 4.8. The blue particles are the ones still bound to the cluster. The final position of the cluster differs from the previous model, because of the difference in initial mass and different mass

loss. However, this does not affect the properties of the cluster itself within the half-mass radius (the orbits being similar and the final distances too).

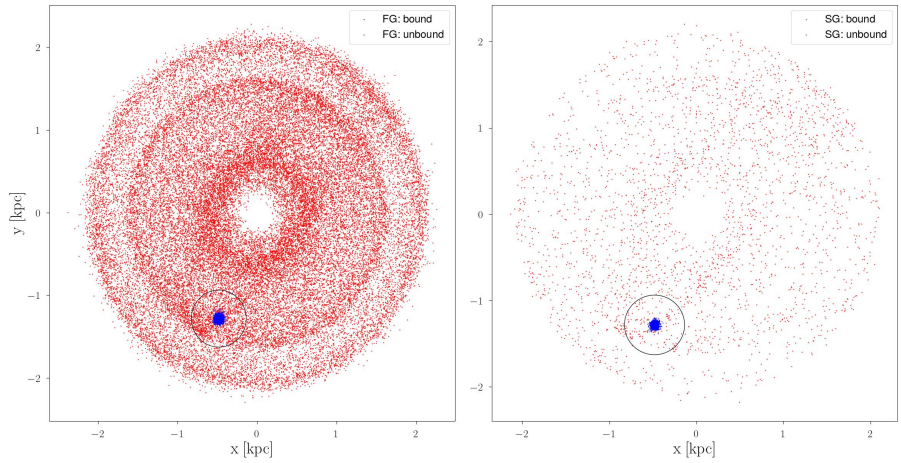

Figure 4.8: Motion of Terzan 5-like cluster around the Galaxy for the second model, reproducing scenario II. In blue the bound particles are shown. The black circle highlights the distance of the most distant bound star belonging to the cluster. FG (left panel) is the first generation, corresponding to MP in Terzan 5, while SG (right panel) is the second generation or MR in Terzan 5.

The bound particles were used to compute the density of the Terzan 5-like cluster, analogously to what was done in Section 3.4 for Terzan 5. The result is shown in Figure 4.9.

I then plotted the density maps of the two populations separately, as I did for Terzan 5 in Section 3.4. On the abscissa and ordinate, there are the projected 2D stellar coordinates relative to the cluster center. The color levels are indicative of the stellar density, based on the 2D binned density estimated by defining a grid of bins within which the number of enclosed stars was calculated, to define the contour lines. The color bar is given in logarithmic scale. The density maps on the xy plane for the FG (MP for Terzan 5) and SG (MR for Terzan 5) are shown in Figure 4.10.

From the density profiles, we see that the SG is denser than the FG within $r \sim 10$ arcsec. The maps instead show that the SG is more concentrated towards the center. This peculiarity in the density of the particles for this Terzan 5-like cluster is well within the half-mass radius, which was calculated for the entire Terzan 5-like cluster and for the two populations separately. The results are listed in Table 4.8.

Table 4.8: Half-mass radius for the entire Terzan 5-like cluster, the FG (MP in Terzan 5) and the SG (MR in Terzan 5) separately.

	$r_{h,tot}$	$r_{h,FG}$	$r_{h,SG}$
[deg]	0.053	0.056	0.047
[pc]	6.80	7.16	6.09

Further on, I investigated the internal dynamics of the Terzan 5-like cluster,

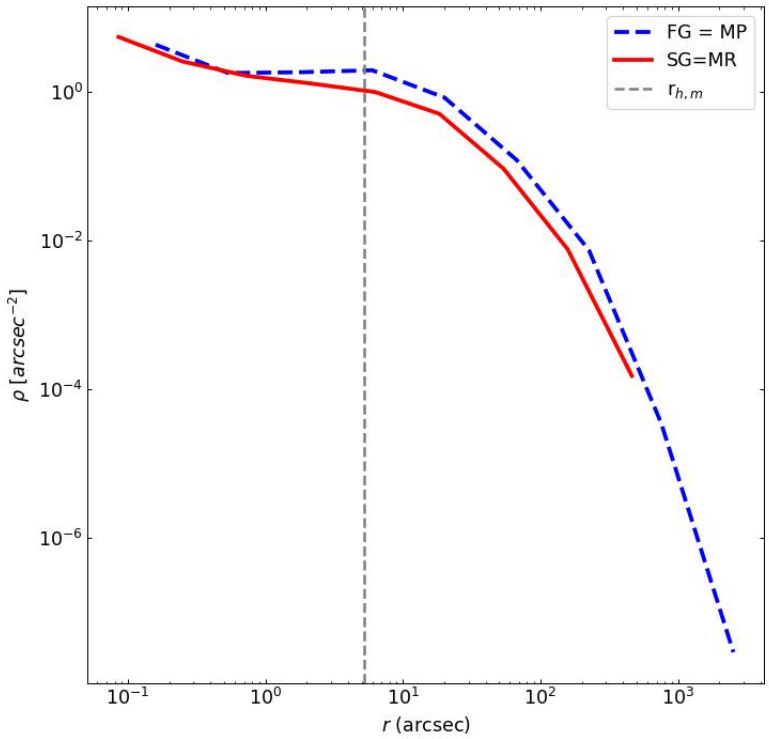

Figure 4.9: Density profile of the stars in the second model Terzan 5-like cluster with respect to the distance from the center in arcseconds. The blue line corresponds to the FG (MP in Terzan 5), the red line to the SG (MR in Terzan 5). The grey dotted line highlights the logarithmic value of the total half-mass radius of the cluster in arcseconds.

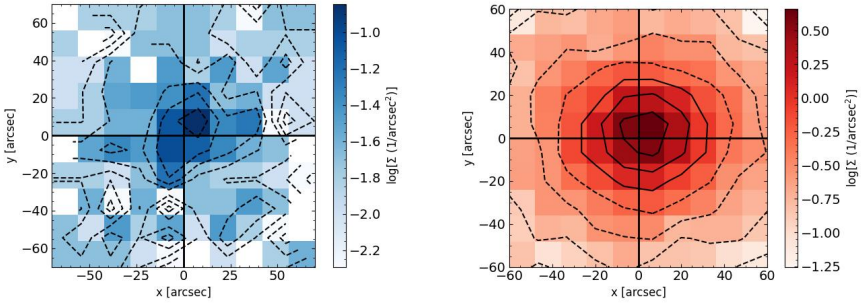

Figure 4.10: Density maps of the FG (left panel) SG (right panel) populations in second model Terzan 5-like cluster, on the xy plane.

such as I did for Terzan 5 and described in Section 3.5 and for the first model. The analytical process is identical to the one described for the previous model. The proper motions $\mu_\alpha cos\delta$ and μ_δ are shown in Figure 4.11.

The obtained velocity dispersion profiles for this model are represented in Figure 4.12.

The radial velocity dispersion of both populations in Terzan 5-like cluster reaches its maximum value at around 0.4 km/s in the innermost analyzed

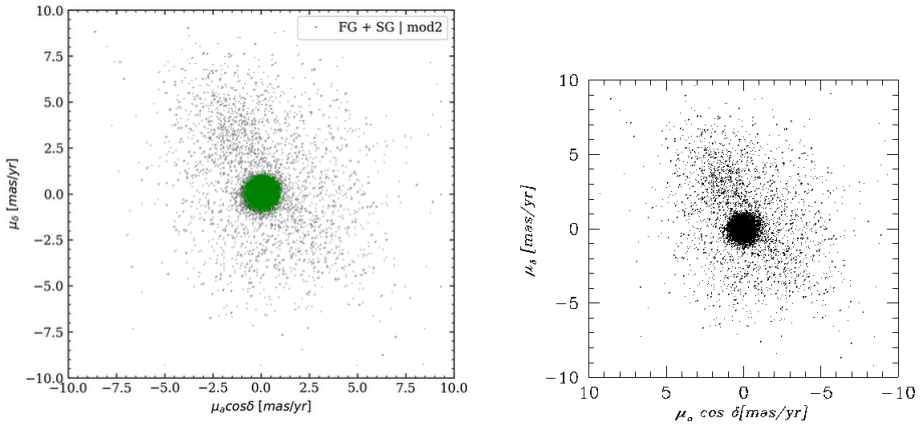

Figure 4.11: Proper motion distributions for the second Terzan 5-like cluster along the RA and DEC directions, with Terzan 5 observational results in grey in the background. On the left the proper motions of Terzan 5 are reported, to use as a comparison.

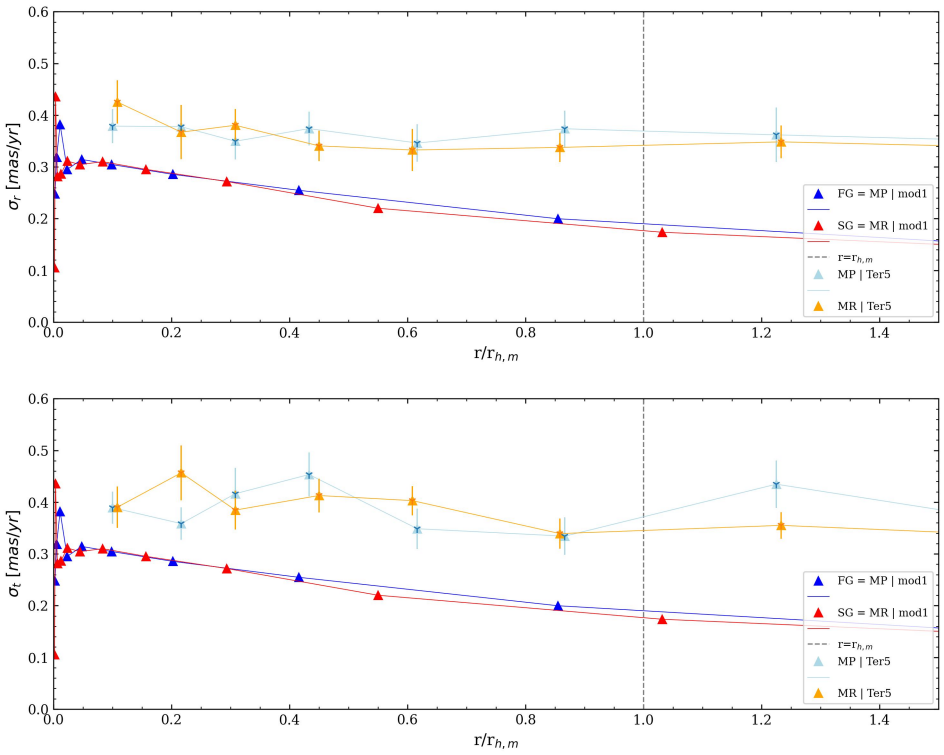

Figure 4.12: Average radial (upper panel) and tangential (lower panel) velocity dispersion profile as a function of the radial distance from the Terzan 5-like cluster center, in the second model. The radial quantity is normalized over the total half-mass radius equal to 0.053 deg. The grey dotted line highlights $\frac{r}{r_{h,tot}} = 1$. The observational results are shown too: MP population in light blue, MR in orange. They are normalized to the half-light radius of Terzan 5, equal to 0.012 deg.

region, the tangential one at 0.3 km/s. Both of their decline in the modeled cluster outskirts, as for the real cluster. The overall trend is consistent with

the observational results.

I then computed the radial dependence of the deviation from the isotropy of each population. I quantified the parameter β describing anisotropy as explained in Section 3.5.3. The anisotropy parameter for the populations of the second model Terzan 5-like cluster is plotted as a function of the radial distance from the cluster center in Figure 4.13. The radial coordinate is normalized to the half-mass radius $r_{h,tot}$ (see Table 4.8).

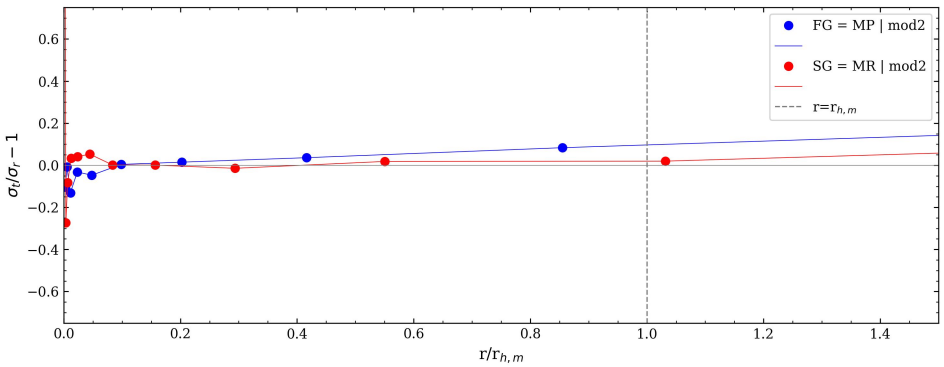

Figure 4.13: Anisotropy parameter β showing the deviation of isotropy for the MP (in blue) and MR (in red) populations in the second model Terzan 5-like cluster. The radial quantity is normalized over the half-mass radius equal to 0.053 deg. The grey dotted line highlights $\frac{r}{r_{h,tot}} = 1$.

The results show that the studied populations in the Terzan 5-like cluster are both radially and tangentially consistent with isotropy. This is true in the central region of the cluster (as before, the spikes near the very center are caused by the limited accuracy of the model), while in the outer cluster regions we observe a deviation from the isotropy and the FG-MP and SG-MR populations show different behaviors, with the FG being more tangentially anisotropic than the SG. The comparison of these results with the observed ones for Terzan 5 is shown in Figure 4.14.

The second model Terzan 5-like cluster is generally consistent with zero anisotropy. The general trend of the modeled data points seems to reproduce well enough the observational data; additionally, we observe a slight tangential anisotropy for the FG-MP population, as in Terzan 5. More details are given in Section 5.

4.4.3 Model 3: scenario III

In the third and last model, the final cluster is the result of a merging between an FG and an SG almost 4.5 Gyr ago. This corresponds to Scenario III described in Section 1.3.3, which is not supported by any study in the literature so far. The initial conditions of the King model for the two populations are the same for the previous models.

I analyzed the last snapshot of the simulation, as in the previous models. In this case, we let the FG cluster evolve internally on its orbit around the Galactic

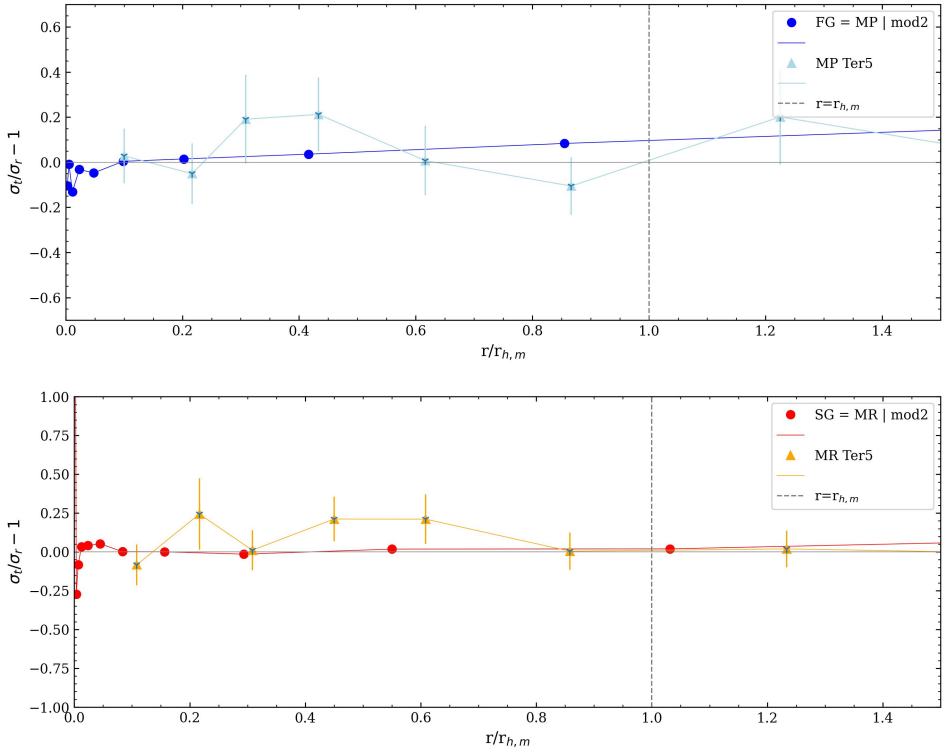

Figure 4.14: Anisotropy parameter β showing the deviation of isotropy for the MP (in blue) and MR (in red) populations in the second model Terzan 5-like cluster. In the upper panel, the cluster-like results are compared with the observed ones for the FG-MP population, in the lower panel the same is done with the SG-MR population. The radial quantity is normalized over the half-mass radius equal to 0.053 deg. The grey dotted line highlights $\frac{r}{r_{h,tot}} = 1$.

center for 7.5 Gyr and then added the SG component on a circular orbit around the FG and let them merge. This process happens quickly and leaves us with a new cluster with two different populations. In Table 4.9 the masses of the cluster, the FG, and the SG (considering just bound stars) are given. Here we see the FG consists in the 12% of the total mass of the cluster. This is not consistent with Terzan 5. Additionally, the total mass of the final cluster is not compatible with Terzan 5's mass equal to $9.35 \pm 0.69 \times 10^5 M_\odot$ (Baumgardt et al. 2021). This suggests the model is not reproducing the observational results: the SG is probably too compact and does not lose enough mass in the 4.5 Gyr of co-evolution with the FG, that instead in the previous 7.5 Gyr had already lost a significant amount of mass (the reason why now the mass fraction of the FG is so small). We will run future models with a more compact FG and a less compact SG to verify if we can reproduce the mass properties of the cluster also in this merger.

The center of mass, calculated as explained in Section 4.3.3, is different for the entire Terzan 5-like cluster and the two populations separately. The coordinates of the position and velocity of each center are all given in Table 4.10. The distance in parsec between the center of mass of the MP and of the MR

Table 4.9: Mass values in the final snapshot after 12 Gyr of the Terzan 5-like cluster in model 1.

$M_{tot,f}$ $[M_\odot]$	M_{FG} $[M_\odot]$	M_{SG} $[M_\odot]$
6.36 $\times 10^5$	7.80 $\times 10^4$	5.58 $\times 10^5$

populations is 1.21 pc, which is large with respect to the core radius and half-light radius of Terzan 5 (Baumgardt et al. 2021) and corresponds to the 30% of the total half-mass radius of this cluster.

Table 4.10: Center of mass for the entire Terzan 5-like cluster and the two populations separately in model 1. FG is the first generation stellar population, corresponding to MP in Terzan 5, while SG is the second generation, corresponding to MR.

	CM_{tot}	CM_{FG}	CM_{SG}
x_{CM} [pc]	1754.24	1753.88	1754.28
y_{CM} [pc]	-512.09	-513.09	-511.95
z_{CM} [pc]	121.70	121.65	121.71
$v_{x_{CM}}$ [km/s]	-45.64	-45.52	-45.66
$v_{y_{CM}}$ [km/s]	-31.34	-31.30	-31.35
$v_{z_{CM}}$ [km/s]	-27.55	-27.61	-27.54

The position of the cluster in the Galaxy at the end of the simulation (running from 0 up to 12 Gyr) is shown in Figure 4.15. The blue particles are the ones still bound to the cluster.

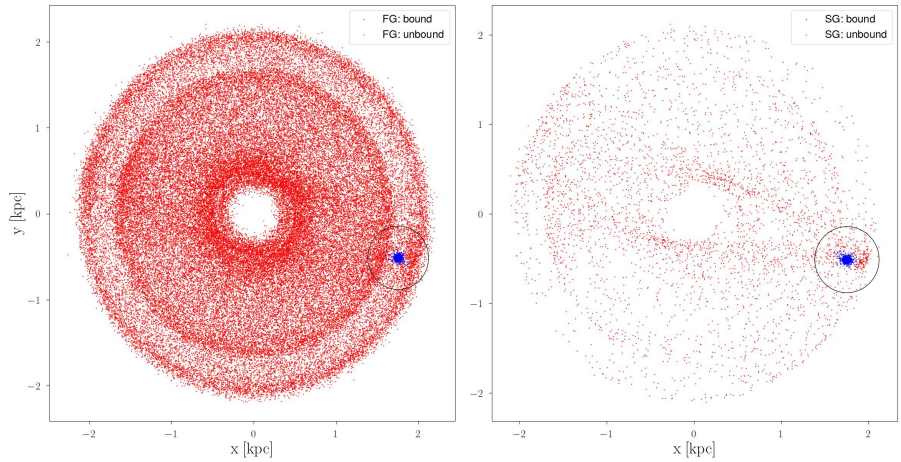

Figure 4.15: Motion of Terzan 5-like cluster around the Galaxy for the third model, reproducing scenario III. In blue the bound particles are shown. The black circle highlights the distance of the most distant bound star belonging to the cluster. FG (left panel) is the first generation, corresponding to MP in Terzan 5, while SG (right panel) is the second generation or MR in Terzan 5.

The bound particles were used to compute the density of the Terzan 5-like cluster, analogously to what was done in Section 3.4 for Terzan 5. The result

is shown in Figure 4.16.

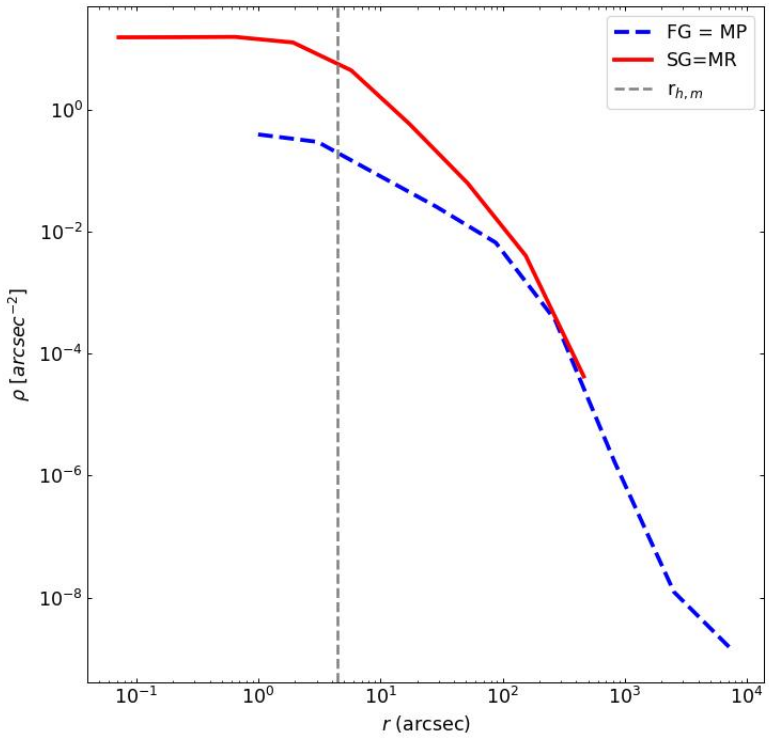

Figure 4.16: Density profile of the stars in the third model Terzan 5-like cluster with respect to the distance from the center in arcseconds. The blue line corresponds to the FG (MP in Terzan 5), and the red line to the SG (MR in Terzan 5). The grey dotted line highlights the logaritmic value of the half-mass radius of the cluster in arcseconds.

I then plotted the density maps of the two populations separately, as I did for Terzan 5 in Section 3.4. On the abscissa and ordinate, there are the projected 2D stellar coordinates relative to the cluster center. The color levels are indicative of the stellar density, based on the 2D binned density estimated by defining a grid of bins within which the number of enclosed stars was calculated, to define the contour lines. The color bar is given in logarithmic scale. The maps on the xy plane for FG (MP for Terzan 5) and SG (MR for Terzan 5) are shown in Figure 4.17.

From the density profiles and density maps, we see that the SG is denser than the FG for $0.1 < r < 10^3$ arcsec, i.e. not just in the very center of the cluster, but also in the outer part. Moreover, as the maps show, the SG appears to be significantly more concentrated than the FG towards the cluster center. This peculiarity in the density of the particles for this Terzan 5-like cluster is well within the half-mass radius, which was calculated for the entire Terzan 5-like cluster and for the two populations separately. The results are listed in Table 4.11.

At this point, I investigated the internal dynamics of the Terzan 5-like cluster, such as I did for Terzan 5 and described in Section 3.5 and for the first and

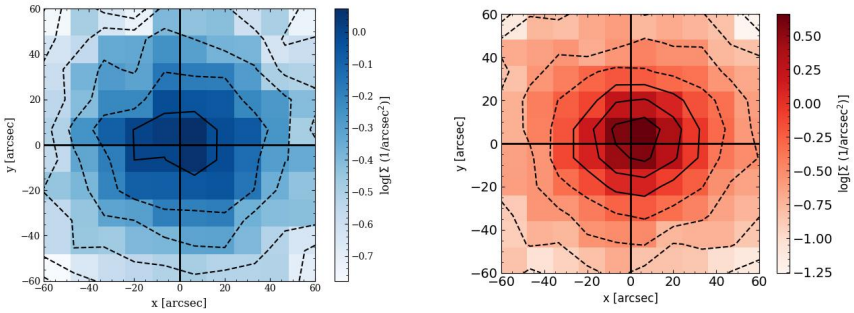

Figure 4.17: Density maps of the FG (left panel) SG (right panel) populations in third model Terzan 5-like cluster, on the xy plane.

Table 4.11: Half-mass radius for the entire Terzan 5-like cluster, the FG (MP in Terzan 5) and the SG (MR in Terzan 5) separately.

	$r_{h,tot}$	$r_{h,FG}$	$r_{h,SG}$
[deg]	0.023	0.077	0.019
[pc]	4.15	13.9	3.37

second models. The analytical process is identical to the one described for the previous models. The distribution of the proper motions $\mu_\alpha cos\delta$ and μ_δ is shown in Figure 4.18.

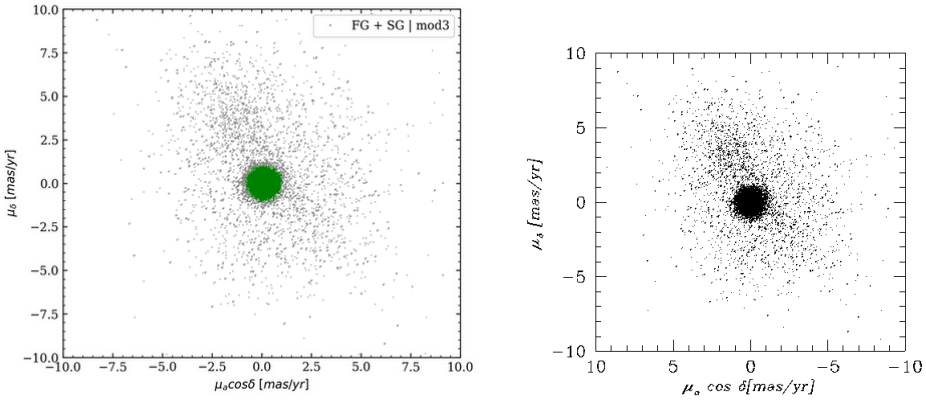

Figure 4.18: Proper motion distributions for the third Terzan 5-like cluster along the RA and DEC directions, with Terzan 5 observational results in grey in the background. In the left panel the proper motions for Terzan 5 from observational data are given, to do a comparison.

The obtained velocity dispersion profiles for this model are represented in Figure 4.19.

Both the radial and tangential velocity dispersions of the populations in this third Terzan 5-like cluster reach their maximum value at around 0.3 km/s, a smaller value with respect to Terzan 5. Both of them decline in the modeled cluster outskirts, but this trend is steeper than for the observational results.

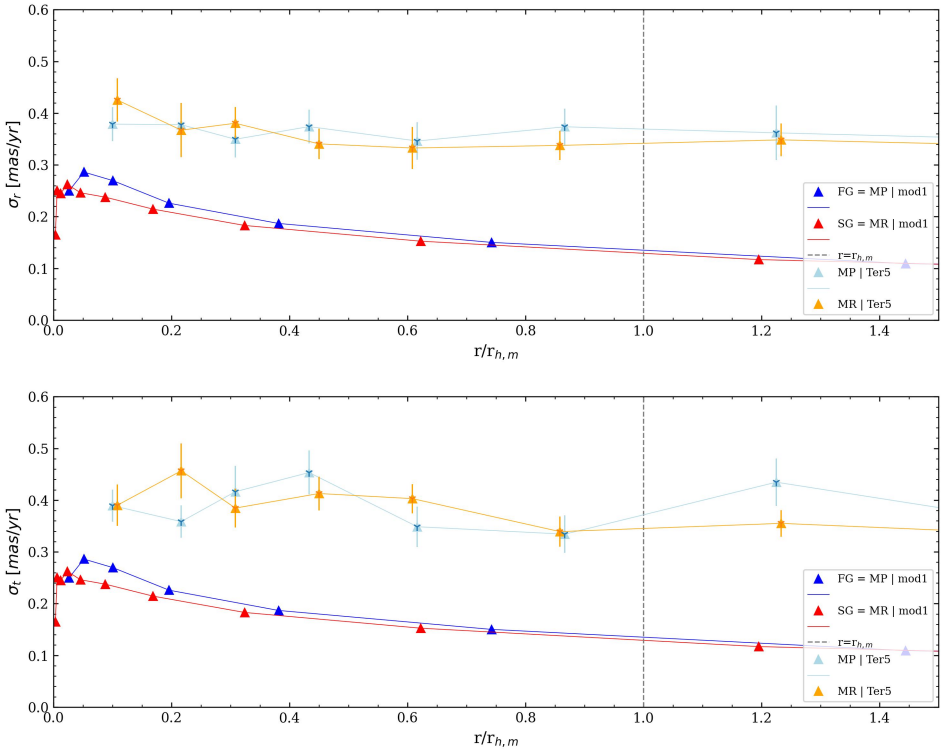

Figure 4.19: Average radial (upper panel) and tangential (lower panel) velocity dispersion profile as a function of the radial distance from the Terzan 5-like cluster center, in the third model. The radial quantity is normalized over the total half-mass radius equal to 0.023 deg. The grey dotted line highlights $\frac{r}{r_{h,tot}} = 1$. The observational results are shown too: MP population in light blue, MR in orange. They are normalized to the half-light radius of Terzan 5, equal to 0.012 deg.

I then computed the radial dependence of the deviation from isotropy of each population. I quantified the parameter β describing anisotropy as explained in Section 3.5.3. The anisotropy parameter for the populations of the third model Terzan 5-like cluster is plotted as a function of the radial distance from the cluster center in Figure 4.20. The radial coordinate is normalized to the half-mass radius $r_{h,tot}$ (see Table 4.11).

The results show that the studied populations in Terzan 5-like cluster at a first sight seem not to be consistent with general isotropy in the $r < r_{h,tot}$ region (similarly to model 2), where there seems to be a small radial anisotropy for SG-MR population in the range $0.4 < r < 1$ and a small tangential anisotropy for FG-MP population for $r > 0.8$ deg. In the outer region, at radii larger than the half-mass radius of the simulated cluster, the tangential anisotropy of the FG-MP population is slightly more pronounced. The comparison of these results with the observed ones for Terzan 5 is shown in Figure 4.21.

The third model Terzan 5-like cluster is generally consistent with zero anisotropy, and the general trend of the modeled data points is not well reproduced the observational data. More details are given in Section 5.

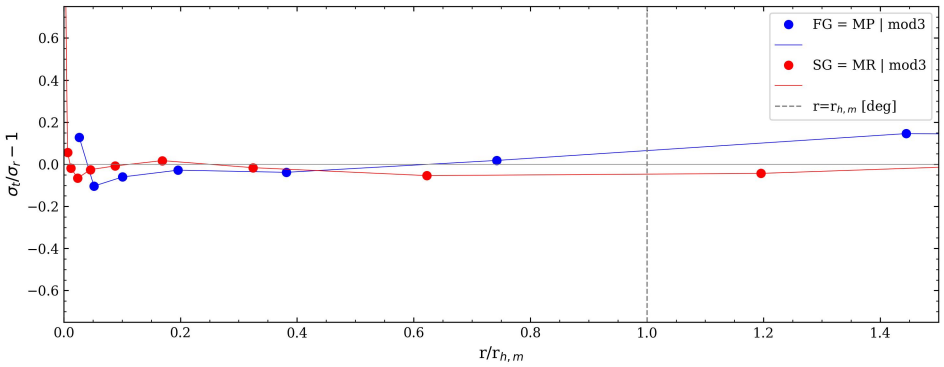

Figure 4.20: Anisotropy parameter β showing the deviation of isotropy for the MP (in blue) and MR (in red) populations in second model Terzan 5-like cluster. The radial quantity is normalized over the half-mass radius equal to 0.023 deg. The grey dotted line highlights $\frac{r}{r_{h,tot}} = 1$.

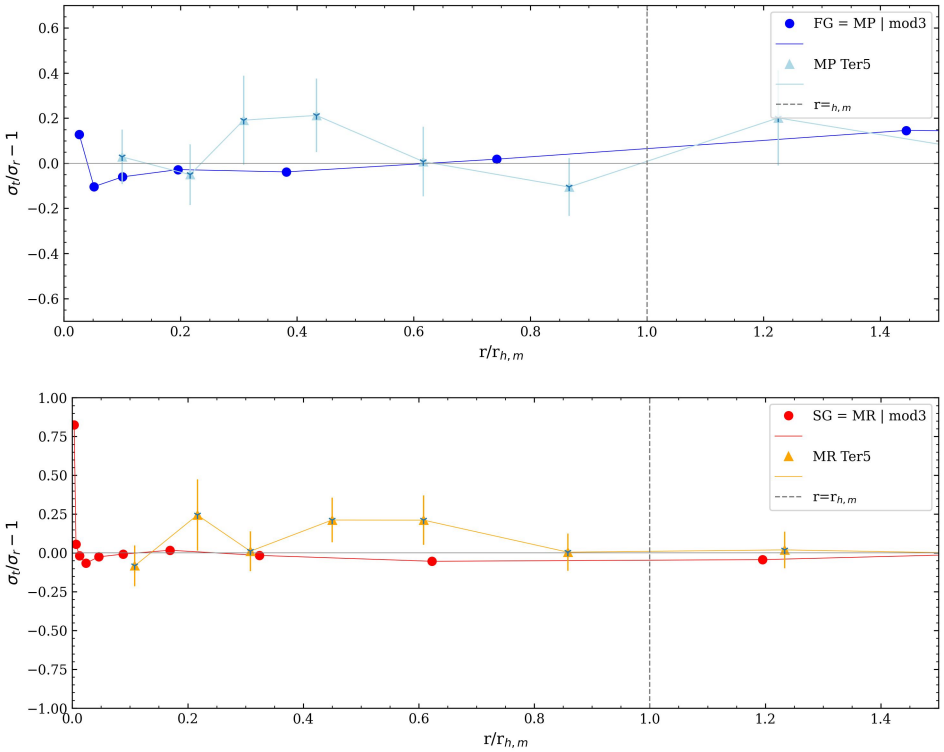

Figure 4.21: Anisotropy parameter β showing the deviation of isotropy for the MP (in blue) and MR (in red) populations in third model Terzan 5-like cluster. In the upper panel, the cluster-like results are compared with the observed ones for the FG-MP population, in the lower panel the same is done with the SG-MR population. The radial quantity is normalized over the half-mass radius equal to 0.023 deg. The grey dotted line highlights $\frac{r}{r_{h,tot}} = 1$.

Chapter 5

Final discussion

In this work, I exploited multi-band photometry obtained from images collected with the ACS/WFC camera on board HST for Terzan 5 in three different epochs and I derived high-precision astrometry and multi-band photometry for all the stars in the field of view. Hence, I obtained an accurate astrometric and a photometric catalog. The data reduction was done by using the methods and computer programs developed by Jay Anderson at the STScI.

By properly combining the stellar positions in images collected at different epochs, I derived the proper motions of all the stars in the field of view of Terzan 5. The vector point diagram of proper motions allowed me to clearly separate the bulk Terzan 5 cluster members from field stars. This information allowed me to derive the CMD of Terzan 5 stars and to correct the photometry for the effect of differential reddening. The magnitudes have been calibrated into the Vega system. The exquisite quality of the photometry allowed me to identify and characterize two distinct red and blue RCs and RGBs, which correspond to stellar populations with different metallicities.

I investigated their radial distribution and confirm that the MR stellar population is more concentrated than the MP one. Moreover, I investigated, for the first time, the internal kinematics of the distinct stellar populations along the line of sight. Specifically, I analyzed the radial and tangential motions of the stars in the cluster, their velocity dispersions, and the anisotropy parameter β. I discovered that Terzan 5 is characterized by an isotropic motion both in the radial and tangential directions and that the MR and MP stellar populations share similar motions. This is something that may be surprising since the cluster has a half-mass relaxation time $T_{r,h} = 2.2 \times 10^9$ yr (Baumgardt et al. 2021) while Terzan 5's age is estimated to be 12 Gyr (Ferraro et al. 2009). Hence, we would expect that Terzan 5 and its stellar populations would retain the signature of deviations from isotropy if present at formation.

To constrain the star formation history of Terzan 5, I compared the observations with simulated GCs. I generated different Terzan 5-like clusters through N-body models corresponding to three different formation scenarios that have been hypothesized for Terzan 5. The comparison between the structural pa-

rameters and internal kinematics obtained within the models and from the observational data follows.

5.1 Structural parameters

The values of the half-mass radius and of the total cluster mass that result from the three simulations of the Terzan 5-like stellar systems are provided in Table 5.1. The half-mass radius ranges from ∼4.2 to 6.8 pc and is larger than the values provided by Baumgardt et al. (2021, 3.8 pc). Such a difference between the simulated and the observed clusters is quite expected because I did not fine-tune the initial parameters of the simulations to match the observations. To minimize the impact of the different scales, I will compare the observed and simulated radial distributions of the proper motions by normalizing the radial distance from cluster center in units of half-mass radii.

The total cluster masses inferred from our simulation range from $\sim$ 1 and $6{\times}10^6 M_\odot$. Our values are somehow in between the value provided by Baumgardt et al. (2021, $9.35 \pm 0.69 \times 10^5 M_\odot$) and by Lanzoni et al. (2010) who derived a mass of $2 \times 10^6 M_\odot$) by assuming a mass-to-light ratio $M/L_{bol} = 3$ (e.g. Maraston 1998).

Table 5.1: Values obtained for the half-mass radius of the three different Terzan 5-like clusters in deg and pc and for their total masses. For Terzan 5, $r_{h,m} = 0.012$ deg (Baumgardt et al. 2021) and $M = 9.35 \pm 0.69 \times 10^5 M_\odot$ (Baumgardt et al. 2021).

Model	**Scenario**	$r_{h,m}$[deg]	$r_{h,m}$ [pc]	M [$M_\odot$]
1	I: Type II globular cluster	0.035	5.459	1.21×10^6
2	II: complex stellar system	0.053	6.80	1.48×10^6
3	III: merging	0.023	4.15	6.36×10^5

However, since the results are compatible in terms of order of magnitude, we can conclude that structurally and dimensionally speaking real and simulated clusters are comparable, allowing for a comparison of their dynamical properties.

5.2 Internal kinematics

To compare the internal kinematics obtained from the three Terzan 5-like models and the real observational results, the χ^2 test was used. It was simply defined as the summation of the squares of the differences between the observed and the theoretical datasets:

$$\chi^2 = \sum_i (O_i - T_i)^2 \tag{5.1}$$

where O_i is the observational dataset (with i the number of measurements) corresponding to Terzan 5 results, whereas T_i is the theoretical dataset of each model separately which was found after linearly interpolating the points (see

the plots in the respective Sections of the models). Assuming this definition and the table of interpretation in M. Loreti "Teoria degli errori e Fondamenti di Statistica", 2006, greater differences between theoretical and observational data should produce a larger χ^2 value. The larger the χ^2 value, the greater the probability that there really is a significant difference. This of course depends also on the number of degrees of freedom, defined as $\nu = i - 1$. Since the three models have all the same degrees of freedom, corresponding to $\nu = 7$, they can be compared straightforwardly.

5.2.1 Velocity dispersions

The results of the χ^2 obtained concerning the velocity dispersions are summed up in Table 5.2 for model 1, Table 5.3 for model 2, Table 5.4 for model 3.

Table 5.2: χ^2 values obtained by the comparison between Terzan 5 observational velocity dispersions dataset and the first theoretical model (corresponding to Scenario I: Type II globular cluster).

Population	ν	χ^2_{tan}	χ^2_{rad}
FG = MP	7	0.2349	0.1981
SG = MR	7	0.2743	0.1905

Table 5.3: χ^2 values obtained by the comparison between Terzan 5 observational velocity dispersions dataset and the second theoretical model (corresponding to Scenario II: complex stellar system).

Population	ν	χ^2_{tan}	χ^2_{rad}
FG = MP	7	0.1698	0.1558
SG = MR	7	0.2032	0.1549

Table 5.4: χ^2 values obtained by the comparison between Terzan 5 observational velocity dispersions dataset and the third theoretical model (corresponding to Scenario II: merging).

Population	ν	χ^2_{tan}	χ^2_{rad}
FG = MP	7	0.3579	0.2974
SG = MR	7	0.4077	0.3117

Choosing 0.05 as a significance value, all these results in terms of χ^2 are acceptable to be compared with the observational dataset, in both radial and tangential cases and for both populations.

Under a purely qualitative point of view, since the normalization to the observational uncertainties was not taken into account, the lowest values for the χ^2 parameter are the ones corresponding to model 2. This model corresponds to two populations which are almost the same age, that are born with a temporal difference of ~ 40 Myr. This refers to scenario II, that describes Terzan 5 as a complex stellar system yet to be entirely studied into details, but not descending from a progenitor which was a building block of the galactic bulge.

5.2.2 Anisotropy

The same reasoning was done concerning the anisotropy parameter β. The χ^2 was calculated for all the three models with respect to the observational results, after a linear interpolation of the points (see plots in respective Sections of Chapter 4).

The results for the χ^2 parameters are listed in Table 5.5 for model 1, Table 5.6 for model 2 and Table 5.7 for model 3.

Table 5.5: χ^2 values obtained by the comparison between Terzan 5 observational anisotropy parameter β and the first theoretical model (corresponding to Scenario I: Type II globular cluster).

Population	ν	χ^2
FG = MP	7	0.1700
SG = MR	7	0.2179

Table 5.6: χ^2 values obtained by the comparison between Terzan 5 observational anisotropy parameter β and the second theoretical model (corresponding to Scenario II: complex stellar system).

Population	ν	χ^2
FG = MP	7	0.1910
SG = MR	7	0.1677

Table 5.7: χ^2 values obtained by the comparison between Terzan 5 observational anisotropy parameter β and the third theoretical model (corresponding to Scenario II: merging).

Population	ν	χ^2
FG = MP	7	0.2215
SG = MR	7	0.2031

Again, the lowest values for the χ^2 parameter correspond to model 2 or model 1. As for the velocity dispersions, the anisotropy of model 3 provides a poorer fit with the observations.

5.3 Conclusions

By combining the information on the kinematics and cluster structure, I conclude that Scenario II, which assumes that Terzan 5 hosts two stellar populations with different metallicities by nearly the same ages, provides the best match with the data. However, it was not possible to properly analyze all combinations of internal parameters, and further investigation on Terzan 5 is needed to better constrain the origin of this enigmatic stellar system. I plan to do this in the next future.

Bibliography

Allen, C., Santillan, A. 1991, Revista Mexicana de Astronomia y Astrofisica, 255, 1991

Anderson, J. & King, I. R. 2000, PASP, 112, 1360

Anderson, J. & King, I. R. 2006, PSFs, Photometry, and Astronomy for the ACS/WFC, Instrument Science Report ACS 2006-01

Anderson, J., King, I. R., Richer, H. B. et al. 2008, ApJ, 135, 2114

Baumgardt, H., Hilker, M. 2018, MNRAS, 478, 1520–1557

Baumgardt, H., Vasiliev, E. 2021, MNRAS, 505, 5957–5977

Bellini, A., Vesperini, E., Piotto, G., et al. 2015, ApJL, 810, L13

Bianchini, P., Ibata, R., Famaey, B. 2019, ApJL, 887, L12

Bianchini, P., van der Marel, R.P., del Pino, A., et al. 2018, MNRAS, 481, 2125

Capuzzo-Dolcetta, R., Mastrobuono-Battisti, A., Maschietti, D. 2011, New Astronomy, 284, 295

Cordoni, G., Milone, A.P., Marino, A.F. 2020, ApJ, 898,147

D'Antona, F., Ventura, P., Caloi, V. et al. 2010, ApJL, 715, L63–L67

Dondoglio, E., Milone, A.P., Lagioia, E. P. et al. 2020, ApJ, 906, 76

Ferraro, F.R., Dalessandro, E., Mucciarelli, A. et al. 2009, Nature, 462, 483-486

Ferraro,F.R., Massari, D., Dalessandro, E. et al. 2016, ApJ, 828, 75

Gaia Collaboration, Brown, A. G. A., Vallenari, A., Prusti, T. et al. 2018, A&A, 616, A1

Harris, W.E. 1996, AJ, 112, 1487

Kormendy, J., Kennicutt, R.C. Jr. 2004, Annual Review of A&A, 42, 603-683

Kwok Sau Fa, I. T. Petron, 2001, eprint arXiv

Lacchin, E., et al. (in preparation)

Lanzoni, B., Ferraro, F.R., Dalessandro, E., Mucciarelli, A. et al. 2010, ApJ, 717, 653

Mackey, A.D., Da Costa, G.S., Ferguson, A.M.N., Yong, D. 2013 ApJ, 762, 65

Maraston, C. 1998, MNRAS, 300, 872

Marino, A.F., Milone, A.P., Yong, D. et al. 2014, MNRAS, 442, 3044

Massari, D., Mucciarelli, A., Ferraro, F.R. et al. 2014, ApJ, 795, 22

Massari, D., Dalessandro, E., Ferraro, F.R. et al. 2015, ApJ, 810, 69

Mastrobuono-Battisti, A., Khoperskov, S., Di Matteo, P., Haywood, M. 2019, A&A 622, A86

Milone, A. P., Marino, A. F., Cassisi, S., et al. 2012a, ApJ, 754, L34

Milone, A. P., Piotto, G., Bedin, L. R., et al. 2012b, A&A, 540, A16

Milone, A. P., Piotto, G., Bedin, L. R., et al. 2012c, A&A, 540, A16

Milone, A. P., Piotto, G., Bedin, L. R., et al. 2012d, ApJ, 744, 58

Nardiello, D., Libralato, M., Piotto, G., et al. 2018, MNRAS, 481, 3382

Origlia, L., Massari, D., Rich, R.M. et al. 2013, ApJL, 779, L5

Origlia, L., Rich, R.M., Ferraro, F.R. et al. 2011, ApJL, 726, L20

Pouliasis, E., Di Matteo, P., Haywood, M. 2017, A&A 598, A66

Plummer, H.C., 1911, MNRAS, 60, 470

Renzini, A., Buzzoni, A., 1986, ASSL, 195-231

Schiavon, R.P., Johnson, J.A., Frinchaboy, P.M. et al. 2017, MNRAS, 66, 1010–1018

Taylor, D.J., Mason, A.C., Schiavon, R.P. et al. 2022, MNRAS, 513, 3429-3443

Webb, J. et al. 2013, ApJ, 764, 124

Yoshida, T. et al. 1991, Die Makromolekulare Chemie, 2317, 2331